Constraining the exhumation history of the north-western margin of Tibet with a comparison to the adjacent Pamir

Shijie Zhang[1,2], Yani Najman[3], Xiumian Hu[2] *, Andrew Carter[4], Chris Mark[5†] & Weiwei Xue[2]

[1] Tourism College, Henan Normal University, Xinxiang, China

[2] State Key Laboratory of Mineral Deposit Research, School of Earth Sciences and Engineering, Nanjing University, Nanjing, China

[3] Lancaster Environment Centre, Lancaster University, Bailrigg, UK

[4] Department of Earth and Planetary Sciences, Birkbeck, University of London, London, UK

[5] Department of Geology, Trinity College Dublin, Museum Building, College Green, Dublin, Ireland

* corresponding author, huxm@nju.edu.cn

[†] now at: Dept of Geosciences, Swedish Museum of Natural History, Stockholm, Sweden.

ABSTRACT

Regional variations in the evolution of the Tibetan plateau has important implications for our understanding of crustal deformation processes. The evolution of the NW margin of the plateau and its transition to the Pamir to the west is one under-studied region. We focus on this region with a multi-technique detrital study of two sedimentary sections in the Tarim Basin. Our provenance data show that an appreciable component of the detrital material in the sedimentary sections was derived from the

Songpan-Ganzi – Tianshuihai composite terrane, with some contribution from the Karakoram and/or the West Qiangtang. Given the proximity of the West Kunlun to the sedimentary sections under study, and its long history of exhumation, this terrane in all likelihood also contributed to the studied successions. Our thermochronological data record phases of exhumation in the hinterland in the Triassic, Early Cretaceous and Oligo-Miocene. Similar to the Pamir, the Triassic and Oligo-Miocene periods of exhumation are attributed to the Cimmerian and Himalayan orogenies respectively. The Early Cretaceous signal may reflect the distal effects of the Lhasa–Qiangtang collision. Coevality with deformation in Pamir suggests a coupled geodynamic system, with retroarc deformation associated with NeoTethyan subduction in the west, and terrane accretion in the east.

How and when the Tibetan plateau developed has important implications for our understanding of crustal deformation processes. Within this framework, a knowledge of both spatial and temporal variability in deformation is important. For example, North–South variation in the degree of inherited crustal strength resulting from Cretaceous deformation has been proposed to influence the degree and extent of plateau uplift that resulted from Cenozoic India–Asia collision (Ding *et al.* 2022). Furthermore, the variation in Cretaceous deformation extent and possibly timing between the Pamir and the Kunlun along the northern margin of the Tibetan plateau illustrates East–West variations, the reasons for which are not well known (e.g. Li *et al*. 2022; Villarreal *et al.* 2023). Furthermore, the degree of previously underestimated pre-Cenozoic deformation is being increasingly documented (e.g. Robinson 2015), impacting estimates of the amount of crustal deformation that must be accounted for in the Cenozoic.

The NW margin of the Tibetan plateau is an understudied region in terms of deformational events, yet knowledge of the evolution of this region is critical to our understanding of the development of the plateau. For example, the documented north–south variation in Tibetan plateau crustal strength resulting from variable Cretaceous deformation as discussed by Ding *et al*. (2022) (see above) is primarily based on the central–eastern rather than northern and western regions of Tibet. Furthermore, the nature of the transition in deformation style between the Pamir to the northwest and Tibet to the northeast (e.g. Villarreal *et al*. 2023), is lacking in detail. It is therefore to this NW region of the Tibetan plateau margin that we turn our attention in this paper.

Various provenance and thermochronological arguments have previously been brought to bear on this discussion. In this paper we compare data from within and outwith the Pamir salient, to advance our understanding of the evolution of the NW margin of Tibet. Our approach involves the interrogation of the sedimentary record on the SW margin of the Tarim Basin which abuts the West Kunlun (WKL) northern margin of the plateau (Fig. 1), using various detrital thermochronological and geochronological techniques. We investigate a new Paleogene section at Kashitashi (Fig. 1A), which is the most eastern section in NW Tibet studied thus far. Additionally, we build on the previous work of Cao *et al.* (2015) applying new techniques to the most easterly studied Neogene section at Sanju (Fig. 1A). This approach allows us to complement bedrock studies by sampling a wider catchment area, and to complement modern river detrital studies, by sampling a longer temporal timescale.

Geological background

The geology of NW Tibet and the Pamir

The NW margin of Tibet east of the Pamir Salient, and the Western Tibet plateau.

The Tibetan plateau lies south of the Tarim craton (Fig. 1). It is made up of a number of terranes (Fig. 1B) which successively rifted from Gondwana, and drifted across the Tethys oceans, to eventually form the southern margin of Eurasia by the Late Cretaceous (Metcalfe 1998; Xiao *et al*. 2005).

In NW Tibet, furthest north is the West Kunlun (WKL), comprised of North Kunlun and South Kunlun, separated by the Kudi Suture / Tam Karaul Fault. The WKL consists of Precambrian metamorphic basement, Palaeozoic and possible minor Mesozoic metasedimentary rocks and Cambrian–Silurian intrusive rocks (Wang *et al*. 2003; Cao *et al*. 2015; Zhang *et al*. 2018; and references therein). The WKL is separated from the terranes to its south by the Karakax Fault. To its south is the composite Songpan-Ganzi – Tianshuihai terrane, consisting of Paleozoic and Mesozoic sedimentary rocks, Cambrian and Triassic plutons and minor Miocene to Quaternary igneous rocks (Deng 1998; Ding *et al*. 2013). South-east of the Songpan-Ganzi – Tianshuihai terrane, is the Qiangtang terrane, which is comprised of Paleozoic–Mesozoic strata, high-pressure metamorphic mélange, ophiolites, and minor Triassic, Cretaceous, and Paleogene intrusive igneous rocks (Wen *et al*. 2000; Ma *et al*. 2017). South-west of the Songpan-Ganzi – Tianshuihai terrane is the Karakoram terrane. The Karakoram terrane, considered to be correlative to the Qiangtang (Robinson *et al.* 2015) comprises Palaeozoic to Mesozoic sedimentary successions, some of which are metamorphosed at some locations (Wen *et al.* 2000), and Cretaceous and minor Paleogene intrusive rocks (Deng 1998). Neogene intrusive rocks are also found west of the Karakoram Fault (Fraser *et al*. 2001).

Collision of the North and South Kunlun closed the proto-Tethys in this region in Palaeozoic times (e.g. Xiao *et al.* 2005). The WKL then represented the southern margin of the Tarim craton of Asia prior to closure of the palaeo-Tethys due to collision with the Qiangtang terrane during the Cimmerian orogeny, probably in the Triassic (e.g. Dewey *et al*. 1988; Ding *et al*. 2013; Kapp & DeCelles 2019). The Songpan-Ganzi terrane consist of Middle–Upper Triassic submarine fan and deep marine facies rocks which formed between the WKL and the Qiangtang terrane during this ocean closure (Ding *et al*. 2013).

Further South, the Lhasa terrane collided with the Qiangtang terrane in latest Jurassic (e.g. Raterman *et al*. 2014; Hu *et al*. 2022) closing the Meso-Tethys along the Bangong–Nujiang Suture. Finally, the Indian plate collided with the Lhasa terrane in the early Cenozoic, along the Indus–Yarlung suture, closing the Neotethys ocean (e.g. Hu *et al*. 2015; Kapp & DeCelles 2019; An *et al*. 2021; and references therein).

The extent to which the Tibetan plateau deformed and rose in the Mesozoic versus Cenozoic is subject to ongoing research (e.g. Raterman *et al*. 2014). Interestingly a recent study by Ding *et al*. (2022) proposes that deformation in the two time periods are intrinsically linked in that the uplift of Tibet post India–Asia collision did not occur as a single entity, or progressively, but instead in piece-meal fashion, influenced by inhomogeneities in the crust inherited from variable levels of Cretaceous deformation.

The Pamir salient

The Pamir salient is, broadly, the western continuation of the NW Tibetan margin (Fig. 1B). It is comprised of the North, Central and South Pamir terranes, separated by the Tanymas and Rushan–Pshart sutures, respectively. The Pamir terranes are separated from the Karakoram terrane to the south by the Wakhan–Tirich boundary Suture Zone (TBZ). The North Pamir consists of the Darvas–Oytag terrane and the Karakul–Mazar terrane. The North Pamir represents the late Paleozoic southern margin of Asia, with the Darvas–Oytag terrane debatably considered to be equivalent to the WKL eastward along strike in NW Tibet, and the Karakul–Mazar terrane equivalent to the Songpan-Ganzi accretionary prism in NW Tibet. The Central and South Pamir are considered to be equivalent to the Qiangtang terrane (Robinson 2015), although the Rushan–Pshart and Wakhan–TBZ sutures in the Pamir do not continue eastward into the Qiangtang terrane; they either terminate at the Qiangtang or merge with the Jinsha and Bangong sutures north and south of the Qiangtang terrane.

How the Pamir salient developed is a subject of debate. Whilst post-Cimmerian Mesozoic deformation in the Pamir has long been recognised, its extent has been consistently under-estimated in early studies (e.g. see review in Robinson, 2015) and its cause ascribed to retroarc deformation associated with subduction of either the Neotethys (e.g. Li *et al*. 2022) or Mesotethys (e.g. Villarreal *et al*. 2023). Furthermore, whilst pioneering work considered the salient developed from a previously linear east–west trending southern margin of Asia as the result of Cenozoic indentation associated with India–Asia collision (e.g. Burtman & Molnar 1993), recent work indicates that the protrusion may be the result of infilling of an irregular coastline of southern Asia. In the latter scenario, the embayment resulted from juxtaposition of the two adjacent Karakum and Tarim cratons between an intra-oceanic arc (Li *et al*. 2020; Rembe *et al*. 2021).

The sedimentary rocks of the SW Tarim Basin

The Cenozoic stratigraphy of the SW Tarim Basin consists of, from oldest to youngest, the Kashi Group (Aertashi, Qimugen, Kalatar, Wulagen and Bashibulake Formations), Wuqia Group (Keziluoyi, Anjuan and Pakabulake Formations), Atushi Formation and Xiyu Formations (Fig. 2). Above the marine Kashi Group, the Wuqia and younger successions are predominantly continental sandstones and mudstones, with predominantly conglomerates at the top of the Xiyu Formation. The Wuqia Group is predominantly fluvial, with some lacustrine and paludal facies, whilst the overlying Atushi and Xiyu formations have been interpreted as alluvial fan facies, with some floodplain and aeolian influence (Zheng *et al*. 2006; Sun & Liu, 2006; Cao *et al*. 2015; Zheng *et al*. 2015; Li *et al*. 2021).

Early work placed the marine Kashi Group as Paleocene to early Oligocene, the Wuqia Group as late Oligocene–Miocene, and the Atushi Formation as Pliocene (e.g. Compiling Group for Xinjiang Regional Stratigraphic Chart 1981; Sun & Liu 2006; Zheng *et al*. 2000). More recently, the western Tarim Basin sediments adjacent to the Pamir have been precisely dated. Biostratigraphic data show the final marine incursion occurred at 37–38 Ma (Bosboom *et al*. 2014), whilst high resolution magnetostratigraphy has placed the top of the Bashibulake Formation at ~35 Ma, the top of the Wuqia Group at ~23 Ma and the top of the Atushi Formation at 15 Ma at Aertashi (Zheng *et al*. 2015; see also Blayney *et al*. 2019). However, lithostratigraphic correlation over long distances is fraught with uncertainty in an active thrust belt setting. With this caveat in mind, we provide below the best age constraints available for our studied Kashitashi and Sanju sections, using published data more proximal to and along strike from our study sites, and augmented by our new data (see below). Furthermore, given this degree of uncertainty, we restrict our depositional age designations to simply “Paleogene” or “Neogene” when used in our later discussion, to avoid over-interpretation of our data.

At our Kashitashi section (Figs. 1C and 2C), the 1:250,000 regional geological map (Shanxi Institute of Geological Survey, 2006) shows the Kashi Group unconformably overlying the Yarkand Group Jurassic strata, and overlain successively by the late Paleogene–early Neogene Wuqia Group and Atushi Formation.

At the Sanju section (Figs. 1D and 2B), Sun & Liu (2006) define the sedimentary succession as consisting of the Pakabulake, Atushi and Xiyu formations, whilst Cao *et al*. (2015) consider only the Atushi and Xiyu formations to be present. These units are unconformably overlain by the Quaternary Wusu Group.

Whilst the final marine incursion, represented by the Bashibulake Formation of the Kashi Group is dated at 37–38 Ma to the west (Bosboom *et al*. 2014), further east in the basin at Keliyang and closer to our Kashitashi study site, the final marine retreat occurred at 41 Ma (Bosboom *et al*. 2014; Sun *et al*. 2016), and the time equivalent facies to the Bashibulake Formation further west are, in the east, continental. Therefore this formation has been placed above the Kashi Group in the Kekeya section (Fig. 2A) by some workers (Clift *et al*. 2017; Zheng *et al*. 2015) and as a non-marine equivalent of the Bashibulake Formation, yet still part of the Kashi Group, by other workers in the region east of Pishan (Compiling Group for Xinjiang Regional Stratigraphic Chart 1981).

Above the Kashi Group, the Wuqia Group facies are continental, predominantly fluvial, basin-wide. At the Kekeya section to the west of our study areas, magnetostratigraphic data (Zheng *et al*. 2000), re-correlated with the benefit of a recently discovered tuff layer, has allowed more accurate dating of the continental units (Zheng *et al*. 2015), further modified in Blayney *et al*. (2019). According to this revised stratigraphic dating at Kekeya: the Xiyu Formation is dated from either 15 Ma (Zheng *et al*. 2015) or 20 Ma (Blayney *et al*. 2019) to top of section at 10 Ma; the Atushi Formation is aged between 20–27 Ma; and the underlying Wuqia Group extends to at least 34 Ma, possibly to >37 Ma, depending on whether the base of the exposed section is considered to be Wuqia Group (Zheng *et al.* 2000) or Bashibulake Formation (Clift *et al*. 2017; Zheng *et al*. 2015 – the Bashibulake is considered to be the base of the exposed section at Kekeya, based on the presence of its muddier facies and evaporites; Fig. 2A). Note that our new data may indicate that the Anjuan Formation extends into the Neogene. The horizontally overlying unconsolidated Wusu Group is considered to be of Quaternary age (Compiling Group for Xinjiang Regional Stratigraphic Chart 1981).

Methods

Rationale and approach

Previous authors (e.g. Li *et al*. 2022, Villarreal *et al*. 2023) have commented that post-Cimmerian pre-Cenozoic deformation is located further north (aka north versus south of the Palaeo-Tethyan suture) and may debatably be older in the Pamirs, compared to Tibet. In NW Tibet, the majority of previously published data has been obtained from locations close to the Pamir salient; it is therefore difficult to distinguish between Pamir and Tibet tectonic influences in those regions. We chose the most eastern sedimentary section of the WKL in NW Tibet for our study of Paleogene sedimentary rocks at Kashitashi (fig. 1A), as well as adding to data with new analysis types at the previously studied Neogene Sanju section, where only zircon U–Pb and FT analyses had previously been undertaken (Cao *et al*. 2015). We chose to study Cenozoic siliciclastics to obtain a more comprehensive temporal view compared to modern river sample analyses, and a more comprehensive spatial view compared to bedrock data. We carried out low temperature thermochronological analyses to determine exhumation of the source region, and geochronological analyses to determine provenance in order to determine from what terranes the exhumational data pertained to.

Detrital data from both the Cenozoic sedimentary sections and modern rivers were collected at both locations. The composite Kashitashi section (sections A, B, C in Fig. 1C) was logged and data recorded (Figs. 2 and 3), but logging was not required for the Sanju section as this has already been undertaken by previous workers (Sun & Liu 2006). Data include petrography, zircon and rutile U–Pb age determination, the former also with Hf isotopic characterisation, zircon fission track (ZFT) double dated with U–Pb, and apatite fission track (AFT). Since ZFT double dated with U–Pb data are already available from the Neogene Sanju section (Cao *et al*. 2015), we utilised these data in our study, rather than replicating analyses. Analyses were carried out at a number of laboratories, and full methodologies are given in Supplementary Info 1. Full sample information is given in Supplementary Info 2.

Petrography

Fifteen sandstones were selected for modal analysis, 12 from the sedimentary sections as shown in Fig. 2, and three modern river sands, 15YK01 and 15YK02 at Kashitashi, and SA17 at Sanju, as shown in Fig. 1A. Approximately 400 points were counted for each sample, following the modified Gazzi–Dickinson method, in which crystal grains larger than 62.5 um within a lithic fragment are counted as monocrystalline grains (Ingersoll *et al*. 1984).

Zircon U–Pb analysis

Five samples were analyzed for zircon U–Pb dating. Separated zircon grains were handpicked, mounted in epoxy resin, and polished. Five of the samples were analysed by LA–ICP–MS at the State Key Laboratory of Geological Processes and Mineral Resources, China University of Geosciences, Wuhan. U–Pb analyses were performed using an excimer laser ablation system (GeoLas 2005) coupled to an Agilent 7500a ICP–MS. Standard 91500 was used as an external standard for U–Pb dating, and Standard GJ-1 was analyzed as the internal standard (Wiedenbeck *et al*. 1995; Jackson *et al*. 2004).

An additional 5 samples were selected for zircon U–Pb double dating with fission track analysis. The samples were analysed for U–Pb dating by LA–ICP–MS at the State Key Laboratory of Mineral Deposits Research (MiDeR), Nanjing University. Analysis was performed using a New Wave UP193 laser ablation system coupled to an Agilent 7500a ICP–MS. Standard GJ-1 was used as an external standard for U–Pb dating, and zircon standard Mud Tank was analysed as the internal standard (Gain *et al*. 2019).

Zircon Hf analysis

In situ zircon Hf isotope analysis of three samples (one modern river sample at Sanju located on Fig. 1A, and two samples from the Kashitashi section as shown on Fig. 2) followed U–Pb dating, using a Neptune (Plus) MC–ICP–MS attached to a New Wave ArF 193 nm laser ablation system at the State Key Laboratory of Mineral Deposits Research (MiDeR), Nanjing University. The two zircon reference materials of Mud Tank and 91500 were analysed to correct for instrumental mass bias and depth-dependent inter-element fractionation.

Rutile U–Pb analysis

Seven samples (6 from the sedimentary sections as shown on Fig. 2, and one modern Sanju River sample located on Fig. 1A) were analyzed at Trinity College Dublin, Ireland. Rutile grains were mounted in epoxy resin, ground to expose internal surfaces, and polished. Analyses were conducted using a Photon Machines Analyte Excite 193 nm ArF Excimer laser ablation system with a Helex 2-volume ablation cell coupled to an Agilent 7900 quadrupole ICP–MS. Repeated measurements of the primary R10 and the secondary R19, RZ3, PCA-S207, and Sugluk-4 natural rutile standards were used to correct for downhole U–Pb fractionation, mass bias, and intra-session instrument drift (Bracciali *et al*. 2013; Luvizotto *et al*. 2009; Shi *et al*. 2012).

Fission track analysis

Five apatite separates (samples located on Fig 2) and six zircon separates (5 located on Fig. 2, plus modern Sanju River sand, located on Fig. 1; these same samples being double dated with U–Pb, see above) were analysed for fission track analysis at University College, London, UK. The separated apatite and zircon grains were mounted in araldite and PTFE respectively, ground to expose internal surfaces, and polished. Then they were etched used 5N HNO^3 at 20°C for 20 s (apatite) and a binary eutectic of KOH:NaOH at 225°C for between 6 and 48 h (zircon) to reveal the spontaneous fission-tracks respectively. Etched grain mounts were packed with mica external detectors and corning glass (CN5 for apatite and CN2 for zircon) dosimeters and irradiated in the FRM 11 thermal neutron facility at the University of Munich in Germany, with fluences of 1.2×10^{16} ncm^{-2} (apatite) and 1.25×10^{15} ncm^{-2} (zircon). Following irradiation the external detectors were etched using 48% HF at 20°C for 25 minutes. Sample ages were determined using the zeta calibration method and IUGS recommended age standards (Hurford 1990).

Results

Description of the Kashitashi section

Our new Kashitashi section is a composite of Sections A, B and C as located on Fig. 1C and illustrated in Fig. 2C. Section A is 593 m thick and is comprised of the uppermost Kashi Group and Keziluoyi Formation. Red coloured thin to thick beds are comprised of claystone, siltstone and fine sandstone with minor medium sandstones and intraformational conglomerate. Section B is 230 m thick and is comprised of the upper part of the Keziluoyi Formation and Anjuan Formation. Red coloured thin-thick beds are predominantly comprised of siltstone and fine sandstone with less common medium sandstone and claystone. Section C is 310 m thick and is comprised of the Pakabulake Formation. It consists of thin–thick bedded red coloured claystone, siltstone, fine to coarse sandstone and matrix-supported conglomerate with angular to well-rounded clasts up to 15 cm in length. A number of sedimentary structures, such as channelization and bioturbation, were observed, as illustrated in Fig. 3.

Petrography

Conglomerates

Conglomerates are first recorded at the top of the Kashitashi Section. (Section C, Fig. 2 Pakabulake Formation). Clasts are dominated by granite, with subordinate sedimentary (both clastic and carbonate) clasts. By contrast, the conglomerates in the Sanju section are dominated by sandstone clasts. Additionally, limestone clasts are significant in the Atushi Formation conglomerates, whilst schist clasts and a small proportion of granite clasts are recorded in the Xiyu Formation conglomerates (Fig. 2).

Sandstones

Framework modes (Fig. 4) show that samples are of feldspatho-litho-quartzose, feldspatho-quartzo-lithic and quartzo-lithic in composition (for sandstone classification and nomenclature refer to Garzanti (2019)). Samples from Xiyu and Atushi formations in the Sanju section contain less feldspar compared to the Kashitashi region (samples from Keziluoyi, Anjuan and Pakabulake formations) and modern river sands, which include both our own data and published data (Graham *et al*. 1993; Rittner *et al*. 2016).

Felsic volcanic fragments dominate the lithic component of the Kashitashi region both in section and in the modern rivers draining into the area predominantly from the South Kunlun (samples 15YK01 and 15YK02, from an upstream Yulongkashi River tributary; Figs. 1, 4, and Supplementary Info 3). Sedimentary and metamorphic lithic fragments are more prevalent in the Sanju section and modern rivers that drain more terranes, e.g. both South and North Kunlun (Sanju River, samples SA17 and 55) and the Songpan-Ganzi – Tianshuihai terrane (Yulongkashi downstream, sample 50; Kalakashi River, samples 35 and 54; Figs. 1 and 4).

Full petrographic data and thin section photomicrographs are presented in Supplementary Info 3.

Zircon U–Pb with Hf characterization

Overall, the detrital zircon ages range from 10 Ma to nearly 3000 Ma. All samples from the Sanju and Kashitashi sections have a predominance of grains lying within the range of 200–300 Ma and 400–500 Ma (Fig. 5). The only exception is the modern sand from Sanju River, where the majority of grains lie between 500–600 Ma. In all samples, older grains stretch back to >2000 Ma, with poorly defined greater concentrations between 600–1000 Ma and 1700–2000 Ma. Paleogene grains are sporadically present in both sections. Neogene and Cretaceous grains are also present in the Sanju section. Cretaceous grains are also present in the Sanju modern river sand. Full data are presented in Supplementary Info 4. Detrital zircon spectra from samples from the Paleogene and Neogene sections, and their potential source regions are shown in Fig. 5.

Of the zircons analyzed for Hf isotopes, only three zircon grains with Paleogene ages were analysed, and they yielded slightly positive εHf(t) values ranging from 0 to +2. The εHf(t) values of Cambrian – Triassic zircons ages range widely but are mainly between +10 and -10 (Fig. 6). Full data and plots are presented in Supplementary Info 5.

Rutile U–Pb

Overall, grains range in age from 10 to >2000 Ma (Fig. 7). All samples from the Kashitashi and Sanju sections, and the Sanju modern river sand, have a major peak between 400–500 Ma. In addition: all formations have numerous grains extending to 1000 Ma, except the Xiyu Formation where older grains are rare, and Sanju modern river sand where such grains are absent; grains in the range 100–200 Ma are sporadically recorded; minor Cenozoic grains are present in the Sanju section and Sanju modern river sand. Full data are presented in Supplementary Info 6.

Zircon fission track with U–Pb double dated grains

Data from double-dated zircons from our four new samples from the Wuqia Group of the Kashitashi section and modern river sand from Sanju River were combined with published data from the Sanju section (Cao *et al*. 2015) in Fig. 8. Following the approach of Cao *et al*. (2015), a subset of those ZFT data, namely only those grains where the ZFT age is younger than U–Pb age and therefore indicative of an exhumational rather than volcanic ZFT age, were then deconvolved into populations using RadialPlotter (Vermeesch 2009). These are presented as radial plots (Fig. 9). Full data are presented in Supplementary Info 7 and 8. For our new samples, zircons were dominated by old grains with track densities too high to count. Of the populations with countable tracks, the most significant population is broadly of Triassic ZFT age, present in both Kashitashi region, Sanju section, and the modern Sanju River. Only one sample, A2-163 from the Pakabulake Formation, has a Cretaceous signal. Of the Cenozoic populations, Paleocene–Eocene populations are recognised in both sections, whilst late Oligocene–early Miocene populations are only recorded in the Sanju section and modern river, as to be expected given the Paleogene age of the Kashitashi section. The exception to this is sample KE210 from the Kashitashi section, which has a dominant Neogene aged population which we tentatively interpret as partially reset due to circulating hot fluids associated with late-stage fault activity (see further discussion below).

By comparison with U–Pb ages for double dated grains, the grains with Triassic fission track ages are comprised of both a volcanic component with similar U–Pb ages to their FT ages, and a population with older U–Pb ages stretching back to the Precambrian indicating that their corresponding FT ages are of exhumational origin. The one sample with Cretaceous ZFT ages has corresponding volcanic and exhumational grains but the grain number is very small. Considering the Cenozoic grains, in the Paleogene Kashitashi section, the Paleocene signal in sample BK519 is exhumational, but the number of grains in this population is extremely small whilst the Eocene fission track population in sample BK140 is overwhelmingly of volcanic origin. Both exhumational and volcanic Eocene grains are presented in the Neogene Sanju section. Oligocene–Early Miocene fission track populations, only present in the Sanju section, are predominantly exhumational.

Detrital apatite fission track data

Populations of analysed detrital apatite samples from the sedimentary sections range in FT age between 24.8 Ma and 211 Ma. The modern Yulongkashi River contains a population as young as 5 Ma (Clift *et al*. 2017) (Fig. 10). The lower number of samples analysed per formation precludes a detailed assessment of trends. Triassic, Cretaceous, Eocene and late Oligocene–early Miocene populations are all represented. Full data are presented in Supplementary Info 9. Without the advantage of double dating, as demonstrated for the zircon fission track data, it is more difficult to differentiate between exhumational and volcanic signals. The radial plots of combined zircon and apatite fission track data shown in Supplementary Info 10 show that there are overlapping apatite and zircon fission track ages for a number of age intervals, suggestive of volcanogenic components if the same source is assumed.

Interpretation and discussion

Stratigraphic constraints

Paleogene Kashitashi section

On the basis of the presence of gypsum, typical of the Kashi Group (Bosboom *et al*. 2014), we consider the base of our Kashitashi Section A (Fig. 2) to be the uppermost part of the Kashi Group, the Bashibulake Formation, in line with the 1:250,000 regional geological map (Shanxi Institute of Geological Survey 2006). By correlation with the Kekeya section (Cao *et al*. 2015; Blayney *et al*. 2019; Fig. 2), and knowledge of the timing of final sea retreat in SW Tarim at Keliyang at 41 Ma (Bosboom *et al*, 2014; Sun *et al*. 2016), the Bashibulake Formation can be considered to be 41 Ma at its base to

33–35 Ma at its top. This is consistent with our youngest detrital zircon from the sample of the overlying lowermost Wuqia Group (BK24) dated at 44 Ma, and average weighted mean of the two youngest grains at 45 Ma. Slightly higher up the section, 50 m above the base of the Bashibulake–Wuqia contact, Wuqia Group sample (BK140) records the youngest detrital zircon dated at 41 Ma, and average weighted mean of the five youngest grains at 46.9 Ma. No tighter constraints are provided from zircon U–Pb data up-section, with the youngest grains remaining between 41 Ma and 53 Ma.

Rutile and fission track ages provide no further constraint except for sample KE210 from the Anjuan Formation. Sample KE210 has a dominant young ZFT population at 19±2.2 Ma (83.5%). A second aliquot subsequently measured for double dating yielded an age within error at 16.7±1.4 Ma (97%) (Fig. 9) when modelled as a two-component mixture. The double dating shows that this population is exhumational (Fig. 8). If taken at face value, this population would indicate that the upper Kashitashi section extends into the Neogene, at variance with the currently determined age for the Anjuan and Pakabulake formations. As noted in that section, stratigraphic correlation from well dated magnetostratigraphic sections along strike can be difficult in an active tectonic regime; in that case the stratigraphy may need revision in the light of our new data. However, regarding our new data from Anjuan Formation sample KE210, we note that this Neogene population is not recorded in Anjuan Formation sample KE95 located *c.* 115 m stratigraphically below, and it also seems unlikely that evidence of an exhumational event sufficiently significant to dominate the population at >80% would be completely absent by the time of deposition of the overlying Pakabulake Formation (sample A2-163, Fig. 9), and with a Neogene population only being recorded as a subordinate population (12%) in one middle Miocene sample in the Sanju section. We speculate that this population might be the result of localised partial resetting effected by hot fluids, due to the sample's possible close proximity to a fault; the top of section B lies close to a NW–SE trending gully that can be traced on Google Earth for at least 9 km (from N36°19′37.4″ E79°55′15.2″ to N36°16′34.3″ E80°00′02.3″) and might be a fault since it follows the regional structural trend. More sampling and analysis from the Anjuan Formation at this site will determine whether the depositional age of the formation needs to be refined.

Neogene Sanju section

In the Sanju area, Atushi and Xiyu conglomerates are exposed. This section was originally dated magnetostratigraphically at 2–6.5 Ma (Sun & Liu 2006). Based on the revised age of the Xiyu Formation at Kekeya (<10–20Ma) (Zheng *et al*. 2015), Cao *et al*. (2015) proposed an older age for the Sanju section along strike. They used detrital zircons, double dated with U–Pb and FT techniques to demonstrate a volcanic origin, on which they built their correlation. Yet these grains are not from a tuff. They are detrital volcanic-derived gains which make up only a very small proportion of the zircon population, and thus provide maximum depositional ages only; nevertheless, the youngest grains do young up section (from 19 Ma at the base, to 11 Ma at the top) consistent with direct volcanic input. Using the new correlation of Cao *et al*. (2015), the resulting match with the magnetostratigraphy of Sun & Liu (2006) is poor, but this could be ascribed to the low sampling resolution of the Sanju magnetostratigraphic study. Detrital mineral ages both already published (ZFT from Cao *et al*. 2015) and our new AFT and rutile data, confirm the Neogene status of the Sanju section but provide no tighter constraint than <19 Ma based on the following observations: a youngest ZFT population of 19 Ma from sample TSA02, ~810 m above the base of the magnetostratigraphically dated section; a single rutile grain of 22 Ma and youngest AFT population of 25 Ma in sample SZ04 ~24 m above the base of the dated section; and a youngest zircon U–Pb dated at 19 Ma in sample TSP01 at the base of the measured section, with the next oldest grain dated at 61 Ma (Fig. 2).

With the caveat that exposure is relatively limited, we located the base of the Atushi conglomerates at Sanju between 250–293 m stratigraphic height below the base of the magnetostratigraphically dated section (N37°10′51.90″, E78°30′8.46″ – location of the lowest Atushi Formation conglomerates, 250 m stratigraphic height below the base of the magnetostratigraphically dated section; N37°10′50.58″, E78°30′05.25″ – location of the uppermost Wuqia Group sandstones, 293 m stratigraphic height below the base of the section; Fig. 1D). Therefore, by comparison with the base of the Atushi Formation at the well-dated section at Kekeya (base of Atushi Formation – 27 Ma or 23 Ma; Zheng *et al*., 2015; Blayney *et al*. 2019), we broadly agree with the older age assignment of Cao *et al*. (2015). Yet there remains a mismatch in that if the base of the Sanju conglomerates is taken to be the base of the Atushi Formation (Cao *et al*. 2015), that is dated at Kekeya at 27–28 Ma or 23 Ma, this conflicts with the youngest U–Pb zircon age providing a maximum depositional age from the base of the Sanju section of 19±0.9 Ma (Cao *et al*. 2015), albeit only based on one grain, the significance of which is therefore debatable (Sharman & Malkowski 2020). Given the likely variability of proximal deposits along strike, we concur that the age of the Sanju conglomerates is broadly early-middle Miocene, but the detail is yet to be resolved.

Sedimentary provenance

Constraints from zircon data

The tectonic terranes of Tibet show variations in zircon U–Pb age signatures (e.g. Xue *et al*. 2023), which can be exploited for provenance identification in the basin sediments.

Late Paleozoic to Early Mesozoic zircon populations are common throughout the Kashitashi and Sanju sections (Fig. 5, panels 6 and 7), but not in the Sanju modern river sample which drains only the north part of the WKL (Fig. 5, panel 5). Given that, in the location of our studied sections, Mesozoic plutons are not reported in the WKL hinterland (Fig. 1A), and the WKL metasedimentary rocks are predominantly Paleozoic thus providing no Mesozoic zircons (Fig. 5, panel P5), derivation of the Late Paleozoic to Mesozoic detrital zircons in the Cenozoic sections is unlikely to be from the WKL. The most likely, i.e. proximal, source of these zircons is the Songpan-Ganzi – Tianshuihai terrane, where the sedimentary rocks provide Mesozoic detrital zircons, and Triassic igneous rocks crop out (Fig. 1A) that could be a suitable source for the younger grains of this Late Paleozoic to Early Mesozoic detrital population (see also Fig 5, panel 4). Close similarity to the Songpan-Ganzi – Tianshuihai terrane is also shown in the MDS plot (Fig. 11).

A clear difference in age signature occurs between the top of the Sanju sedimentary section and the modern Sanju river sample (Fig. 5, panel 5) which drains only the WKL, after the Songpan-Ganzi – Tianshuihai contribution has been cut off. There is no diagnostic signature of the WKL which would allow its detritus to be unambiguously recognised in the sedimentary sections. However, given that the WKL was a topographic feature by the end of the Paleozoic (Cao *et al*. 2015), contribution to the sedimentary sections is inevitable.

Minor mid-Cretaceous grains are recorded in the Sanju section, whilst Paleogene zircons (40–62 Ma) are recorded sporadically throughout the Kashitashi and Sanju sections; double dating with fission track indicates a volcanic source for the Paleogene grains in the Paleogene rocks and some of the grains in the Neogene rocks (Fig. 8). Grains of Paleogene age have been documented in the Karakoram and Qiangtang terranes (Deng 1998; Chung *et al*. 2005) and these terranes also make a suitable source for the Cretaceous grains (e.g. Zhuang *et al*. 2018; Liu *et al*. 2017; Fig. 5, Panel 3).

Neogene zircons of volcanic origin, found only in the Sanju section as expected given the Paleogene depositional age of rocks at Kashitashi, are considered by Cao *et al*. (2015) to be most likely derived from volcanics of the Songpan-Ganzi – Tianshuihai (Deng 1998; Li 2008). The younger Neogene grains may be associated with the airfall volcanic event recorded at ~11 Ma (Li 2008; Zheng *et al*. 2015).

Comparison of the detrital Hf data with bedrock sources (Fig. 6) are consistent with our proposed input of both Songpan-Ganzi – Tianshuihai and WKL sources, although the 500 Ma zircon population of the modern river draining the WKL (sample SA17) is not well recorded in the source compilation.

Constraints to provenance from rutile analyses

Our interpretation of rutile provenance is hampered by a paucity of data of the typical rutile signatures of the potential source terranes. The dominant pan-African ~400–500 Ma signal in the Kashitashi and Sanju sections is likely to be widespread and non-diagnostic. Cenozoic grains, although minor in proportion, may be more distinctive. Rutile is typically a metamorphic mineral (Force 1980). However, there is only a sparse record (e.g. Zhang *et al*. 2017) of metamorphism of such age in the WKL, Songpan-Ganzi or Qiangtang terranes in the region, although our sample from the Sanju modern river, which drains the WKL, contains two Cenozoic grains. Cenozoic grains are most likely associated with the widespread Paleogene metamorphism reported from the Karakoram terrane (e.g., Fraser *et al*. 2001) from which similar mineral cooling ages have been reported (e.g. Zhuang *et al*. 2018; Clift *et al*. 2022).

Sedimentary petrography

Petrography shows that the Sanju section tends towards a higher proportion of lithic fragments compared to the Kashitashi section, and of these lithics, a higher proportion are metamorphic and sedimentary compared to volcanic (Fig. 4 and Supplementary Info 3). However, it is not possible to ascertain whether this is a temporal or spatial variation, as no older units were analysed from Sanju, and no younger units were deposited at Kashitashi. What can be said is that the hinterland bedrock signature, as defined by modern river data, mimics the sedimentary rock data. The upstream Yulongkashi, which drains into the Kashitashi region, has similar petrography to the Kashitashi sedimentary rock section, whilst the rivers draining to the front (north) of the range, have signatures similar to the Sanju sedimentary rocks. Interestingly, the change in signature between the Yulongkashi upstream (near Kashitashi area) and Yulongkashi downstream (in the Tarim) is similar to the difference in signature between the Kashitashi and Sanju sections.

Provenance summary

In summary, our data record significant input from the Songpan-Ganzi – Tianshuihai terranes, throughout deposition of the rocks from the Kashitashi and Sanju sedimentary sections. Some contribution from the Karakoram is required to explain the Paleogene rutiles in the Sanju section, and from the Karakoram or Qiantang terranes to explain the Cretaceous zircons in the Sanju section and the Paleogene zircons in the Kashitashi section. The WKL were in all probability also contributing material, as evidenced by the fact that our fission track data from the WKL indicate exhumation since the Triassic and previous research which suggests that, for example, the Tam Karaul Thrust was active since the Mesozoic (e.g. Cowgill 2001). However, the WKL do not have a diagnostic signature that would allow the first appearance of detritus from these terranes to be detected in the sedimentary record using the techniques we have employed. It should also be noted that some material in our younger samples may be recycled through Cretaceous–Paleogene sedimentary rocks deposited on the southern margin of the Tarim Basin, that began to be exhumed since the Late Paleogene (e.g. Cheng *et al*. 2017). However, such deposits, although proximal, are volumetrically relatively minor (Fig. 1A).

Exhumation of the hinterland as determined from thermochronology

Zircon and apatite fission track data are well suited to providing exhumational information in this setting, with double dating of zircons using the U–Pb approach allowing differentiation between volcanic and exhumational ages. We incorporate the previous double dated zircon data from Cao *et al*. (2015) from the Sanju section, but in contrast to those authors, we do not make interpretations using calculation of lag times, due to the uncertainty in the depositional age of the Sanju section, and we do not combine the data with the Kekeya section data because of this. We also incorporate the AFT data from Clift *et al*. (2017) from a sample which, according to the GPS location given, is from the Yulongkashi River (37°5.904′ N 79°57.596′ E).

Triassic exhumation

The previously published ZFT data from the Sanju section (Cao *et al*. 2015) showed a strong Permo-Triassic exhumational event, also now documented by AFT data from one of our Sanju section samples. (Fig. 12). Our new data from the Paleogene Kashitashi section show a strong Triassic, but not Permian, signature recorded in ZFT although not AFT data (Fig. 12). Some zircons with these Triassic ZFT ages must come from the terranes more distal than the WKL in view of their diagnostic Late Paleozoic to Early Mesozoic U–Pb ages (see above). However, some zircons (albeit with ZFT ages in fact of lowermost Jurassic rather than Triassic FT age) with non-diagnostic U–Pb ages, could well be from the WKL as such grains are recorded in the Sanju River which only drains the WKL (Fig. 1). The spatial and temporal prevalence of this signal, as well as occurrence of the signal in ZFT data which records exhumation from greater depth compared to exhumation recorded from AFT data, indicates a widespread and significant event. Previous workers have identified and interpreted this event as associated with Paleotethys closure during the Cimmerian orogeny (Cao *et al*. 2015; Li *et al*. 2019).

Cretaceous exhumation

In the Paleogene Kashitashi section, the Early Cretaceous AFT population is strong in the Keziluoyi Formation and the ZFT signal is strong in the Pakabulake Formation (Fig. 12) where double dating indicates both a volcanic and exhumational component to the ZFT population (Fig. 8). The corresponding zircon U–Pb ages span the Mesozoic to Paleozoic indicating a component of input from terranes more distal than the WKL.

The Cretaceous signal in NW Tibet has previously been interpreted as related to the collision between the Qiangtang and the Lhasa terranes (e.g. Li *et al*. 2019) or associated with the same event as recorded in the Pamir (Cao *et al*. 2015) where there was no collision with the Lhasa terrane, and post-Cimmerian deformation is ascribed to retro-arc deformation (Robinson 2015).

Cenozoic exhumation

Previous work from the NW margin of the plateau shows evidence of exhumation throughout the Cenozoic.

Our data from the Sanju section and modern river concur with and extend previous work. Combining the ZFT data from Cao *et al*. (2015) with our Sanju modern river ZFT data, and our AFT data from the Sanju section with the modern Yulongkashi AFT data from Clift *et al*. (2017) (Fig. 12), we observe that an Oligocene to early Miocene ZFT signal is observed in the Neogene Xiyu Formation. Furthermore, a late Oligocene AFT signal is present from the Upper Oligocene Atushi Formation, accompanied by an early Miocene signal in the modern Yulongkashi river. The double dating from Cao *et al*. (2015) indicates that the ZFT signal is largely exhumational. We suggest the pattern described above reflects progressive unroofing of the hinterland: shallow unroofing is first recorded by the late Oligocene AFT signature in the Atushi Formation; at that time exhumation was not sufficient to exhume zircon with reset ZFT ages. By Xiyu Formation times, exhumation was sufficiently deep to expose zircons with reset Neogene fission track ages. Progressive exhumation continued as recorded by the mid-late Miocene ZFT age recorded in the modern Sanju River and the Pliocene AFT population in the modern Yulongkashi river; however exhumation is not yet sufficiently deep to record such young ZFT ages in the river. Thus a clear exhumational trend is observed from the Oligo-Miocene times onwards.

We note that some of the zircons with Oligo-Miocene FT ages have Triassic U–Pb ages (sample TSX01 and TSA02, Fig. 8), indicating that the Songpan-Ganzi – Tianshuihai, and possibly also West Qiangtang, terranes was exhuming during this period. Cao *et al*. (2015) interpret the Oligo-Miocene zircon fission track population in the Sanju section as derived from the WKL. Likewise, Clift *et al*. (2017) interpret their Miocene and Pliocene AFT population from the Yulongkashi River as derived from the north Kunlun, from which they calculate exhumation rates of the hinterland by 17 Ma at a rate of ~0.2–0.3mm/yr and by 3.7 Ma at rates of ~0.9–1.3 mm/yr. Taking these grain ages to reflect exhumation (it seems unlikely they are volcanic as that would require erosion from a dominant volcanic source because the lag time precludes direct air fall), we concur with the interpretation of exhumation at this time. However, we do not consider the uplifting region was necessarily the North Kunlun, as they proposed, since their GPS reference shows the sample to be from the upper Yulongkashi River which has its headwaters in the Songpan-Ganzi – Tianshuihai terrane (Fig.1A) and the river has Triassic detrital zircons which we interpret as Songpan-Ganzi – Tianshuihai derived. By contrast, Triassic plutons are not prevalent in the North Kunlun drainage area of the Yulongkashi River.

Nevertheless, ongoing thrusting of the WKL is suggested, firstly, by the change in provenance between the top of the Sanju section at 10 Ma, in which detritus from the Songpan-Ganzi – Tianshuihai is still prevalent, and the modern Sanju River in which detritus is solely derived from the WKL (Fig. 5). We interpret the change as due to thrust movement beheading the Sanju headwaters that previously delivered Songpan-Ganzi – Tianshuihai detritus to the Sanju section. Secondly, ongoing thrusting of the WKL is indicated by first appearance of schists in the conglomerates, ~1240 m up-section from the base of the Xiyu Formation section. These clasts are most probably derived from the hanging wall of the Tiklik Thrust where such rocks have been documented (Cheng *et al*. 2017).

Two samples in the Paleogene Kashitashi section have Eocene AFT populations of 53 and 54 Ma which could represent a volcanic or exhumational signal. In the late Oligocene and Neogene Sanju section, there is an AFT signature of 48 Ma, and two samples have a ZFT signature of 50 Ma, of exhumational derivation, and 44 Ma of both exhumational and volcanic origin. The long lag time between Eocene FT age and Oligocene (Kashitashi section) and Oligo-Miocene (Sanju section) deposition precludes any definitive evidence of rapid exhumation. Li *et al*. (2019) considered that Eocene exhumation was subdued, limited to localised regions close to faults, and Cao *et al*. (2015) considered the scattered populations reflected residence in the partial annealing zone prior to exhumation during the Oligo-Miocene event.

A comparison of Cretaceous deformation between the NW margin of Tibet and the Pamirs

Post-Cimmerian pre-Himalayan deformation in the Himalayan–Tibet orogen is understudied, yet increasingly recognised (e.g. Ma *et al*. 2017; Chapman *et al*. 2018; Lai *et al*., 2019; Ma *et al*. 2023). Documentation of such deformation is critical to understanding the degree of geodynamic coupling of Tibet with the Pamir, to determining the amount of shortening that needs to be accommodated in the Cenozoic by India–Asia collision, and to better understand how crustal heterogeneities resulting from variations in the extent of Cretaceous deformation may have influenced Cenozoic uplift of the Tibetan plateau (Ding *et al*. 2022).

Whilst both NW Tibet and the Pamir record the Triassic Cimmerian orogeny and Cenozoic India–Asia collision, Early Cretaceous exhumation differs between the two regions. Both Li *et al*. (2022) and Villarreal *et al*. (2023) note that in the Pamirs, Early Cretaceous deformation is significant in the North Pamir, migrating south by the mid-Cretaceous. By contrast, in Tibet, significant deformation is largely restricted to the Gondwanan terranes south of the Paleo-Tethyan suture (Ding *et al*. 2022) although not entirely so (e.g. Li *et al*. 2019; Liu *et al*. 2005). However whilst the paper of Li *et al*. (2022) emphasises more of a difference in deformational onset between the Pamir, from 140 Ma, and in Tibet, from 105 Ma, and differences in exhumational causes (Lhasa–Qiangtang collision for Tibet versus retroarc deformation associated with Neotethyan subduction for the Pamirs), Villarreal *et al*. (2023) emphasises more the similarities, with a correlation in timing between Tibet and the Pamir illustrating the geodynamic coupling during Meso-Tethyan subduction, and Lhasa–Qiangtang collision, in the east.

Prior to this current work, compiled published data appeared to indicate an abrupt change in the detrital record of Cretaceous exhumation between the Pamir, where Cretaceous cooling ages are common (Fig. 12; Supplementary Info 10), and the adjacent NW margin of Tibet (Fig. 12, Panels E and F from Keliyang and Sanju respectively) where there was a near absence of such ages, as also reflected in the paucity of bedrock ages (Li *et al*. 2019). However, our new data from the Kashitashi section (Fig. 12, panel G) indicates that the previously recorded lack of evidence of Cretaceous deformational signal from the NW margin of Tibet was a data gap rather than being the result of real variation, and the timing of deformation is similar to that of the Pamir (Fig 12, Panel A). In highlighting the similarity in age of Cretaceous deformation between the Pamir and Tibet, our data therefore emphasise the degree of geodynamic coupling proposed by Villarreal *et al*. (2023), with terrane accretion in the east and retroarc deformation in the west, as the Mesotethys subducted. The more restricted extent of Cretaceous deformation along the northern margin of the Tibetan plateau compared to the Pamir likely reflects either (1) slab dynamics in the west, or (2) greater strain partitioning in the east, perhaps related to the narrower width of the Gondwanan terranes in the west, as proposed by Li *et al*. (2022), along strike inhomogeneities in crustal strength as may be caused by the termination of the Rushan–Pshart and Wakhan–Tirich Boundary zone sutures into the Qiantang terrane to the east (Robinson 2015), or the less rigid nature of the Paleozoic margin of the Asian plate, where the Tarim and Karakum cratons were separated by a Carboniferous intraoceanic arc (Li *et al*. 2020; Rembe *et al*. 2021).

Summary and conclusions

Our new provenance and low temperature detrital thermochronological data come from 1) the Kashitashi section: the most easterly Paleogene Tarim Basin sedimentary section thus far studied adjacent to the plateau margin in north–west Tibet, and 2) the Sanju section: the previously studied most easterly Neogene sedimentary section abutting the NW margin of Tibet, to which we add lower temperature thermochronological techniques than previously employed.

Our detrital zircon and rutile U–Pb analyses show that the Kashitashi and Sanju sedimentary sections included considerable input from the Songpan-Ganzi – Tianshuihai terrane, with subordinate input from the Karakoram and possibly the Qiangtang. Input from the WKL was in all probability also significant, since our data show that the area has been undergoing exhumation since the Triassic. However, first arrival of material from the West Kunlun into the basin is not detectable using the techniques we employed.

Similar to the adjacent Pamirs, our low temperature thermochronological data (apatite and zircon fission track) record exhumational events of the contributing hinterland in the Triassic, late Oligocene to early Miocene onwards, and importantly the Early Cretaceous, where such data were previously sparse to absent in this area. Triassic and Cenozoic exhumational signals reflect the Cimmerian and Himalayan orogenies respectively. The Early Cretaceous exhumation in NW Tibet is likely to be associated with the Lhasa–Qiangtang collision. Coevality with the Pamir indicates geodynamic coupling during retroarc deformation associated with Mesotethyan subduction culminating, in the east, with the terrane accretion. The more restricted extent of Cretaceous deformation in NW Tibet compared to the Pamir may reflect slab dynamics in the west, or a higher degree of strain partitioning in the east due to the greater width of the Gondwanan terranes, termination of Pamir sutures, or crustal heterogeneity on the Asian plate.

Acknowledgements and funding

This work benefited from discussions with Fin Stuart, Cristina Persano, Johannes Rembe, Paul Kapp and the assistance of Guillaume Dupont-Nivet, Christopher Kneale and Li Wei in the field. Chris Mark thanks David Chew for facilitating access to analytical facilities. We are grateful for the constructive suggestions from Alexander Robinson and an anonymous reviewer. This work was funded by a Royal Society Newton Fellowship to Xiumian Hu and Yani Najman, the National Natural Science Foundation of China (42102120; 41511130067). Chris Mark was funded by a Starting Investigator Research Grant from Science Foundation Ireland (18/SIRG/5559).

SUPPORTING INFORMATION

Supplementary Info 1 – Analytical methods

Supplementary Info 2 – Sample information

Supplementary Info 3 – Petrography. 3a: data. 3b: Thin-section microphotographs of sandstones and sands from the Kashitashi and Sanju sections and modern rivers.

Supplementary Info 4 – Zircon U–Pb data

Supplementary Info 5 – Zircon Hf data

Supplementary Info 6 – Rutile U–Pb data

Supplementary Info 7 – ZFT data

Supplementary Info 8 – Zircon U–Pb & ZFT double dating data

Supplementary Info 9 – AFT data

Supplementary Info 10 – Radial plots combining all data used in Fig 12.

Figure captions

Fig. 1. (A) Simplified geological map of the West Kunlun orogen and adjacent regions, based on Pan *et al*. (2004). Red stars locate our sedimentary section study areas at Sanju and Kashitashi, blue stars show the locations of Aertashi, Kekeya and Keliyang sedimentary sections, to which we compare our data in Fig. 12. The blue filled circles show the locations of modern river sand petrographic data: Sample 35 is from Rittner *et al*. (2016; also used for zircon U–Pb data), samples 50, 54, 55 are from Graham *et al*. (1993) and samples SA17, 15YK01, 15YK02 (the latter two samples also shown on Fig. 1C) are from this study. Blue filled triangle is the location of modern Yulongkashi River sample (AFT data, Clift *et al*. 2017). Published plutonic zircon U–Pb ages (boxed) are from: 1–Cui *et al*. (2006); 2–Cui *et al*. (2007); 3–Zhang *et al*. (2016); 4–Liu *et al*. (2014); 5–Liu *et al*. (2015); 6–Ye *et al*. (2008); 7–Wei (2018). (B) Simplified map of major tectonic terranes within the region, modified from Robinson *et al*. (2007), with location of Fig. 1A shown by box. Red stars show locations of our studied sections at Sanju and Kashitashi (see Fig. 1A), blue stars indicate locations to which we compare our data in Fig. 12. (C) Simplified geological map of the Kashitashi area, modified after the 1:250,000 regional geological map (Shanxi Institute of Geological Survey 2006), and located by boxed region in Fig. 1A. Three red lines labelled A, B, C locate our measured sedimentary sections at Kashitashi (Fig. 2C). Blue filled circles locate our modern river samples used for petrographic analysis. Original and revised Formation ages as denoted in the key refer to Compiling Group for Xinjiang Regional Stratigraphic Chart (1981) and this study respectively. D: Simplified geological map of the Sanju area (background image is from Google Earth). The starting point of our measured section is the same as that of Cao *et al*. (2015) as depicted on the map. Additionally, we explored a further 350 m down-section to define

the boundary between the Wuqia Group and Atushi Formation. Filled blue triangles denote our sample sites; filled red circles denote previous sample locations of Cao *et al*. (2015).

Fig. 2. (A) magnetostratigraphically-dated Kekeya section (see Fig. 1A for location) adapted in Blayney *et al*. (2019) from Zheng *et al*. (2000, 2015), and reproduced here for reference purposes, to correlate with the Sanju and Kashitashi sections. (B) Stratigraphic log and lithostratigraphic divisions of the Sanju section modified from Sun & Liu (2006) and Cao *et al*. (2015), dated magnetostratigraphically by Sun & Liu (2006), and reinterpreted by Blayney *et al*. (2019). Sample locations with analysis types (greyed out symbols indicate data published in Cao *et al.* (2015), conglomerate clast counts and maximum depositional age (MDA) constraints from this study (thermochronological ages in red text) and from Cao *et al*. (2015) (in green text), R=MDA based on rutile data, Z U–Pb=MDA based on zircon data using a weighted mean where n=>1, ZFT/AFT=MDA based on fission track data. (C) Stratigraphic logs of the Kashitashi sections from this study with sample locations, conglomerate clast counts and maximum depositional age constraints, as constrained by detrital mineral thermochronological ages, as for B, above. Locations of Sections A, B and C are shown on Fig. 1C. Stratigraphic ages of both sections are constrained by the maximum depositional age and comparison with lithostratigraphy in the Kekeya section (Fig. 2A).

Fig. 3. Field photographs of representative sedimentary facies. (A) Gypsum layer, Kashi Group, Kashitashi Section A. (B) Mud rip-up clasts and scoured bases, Keziluoyi Formation, Kashitashi Section A. (C) Interbedded sandstone, siltstone and mudstone, Anjuan Formation, Kashitashi Section B. (D) Desiccation cracks Anjuan Formation, Kashitashi Section B. (E) Dwelling burrow, Anjuan Formation, Kashitashi Section B. (F) Incised channel, Pakabulake Formation, Kashitashi Section C. (G) Interbedded conglomerate and sandstone, Atushi Formation, Sanju Section. (H) Siltstone, Xiyu Formation, Sanju Section. (I) Conglomerate, Xiyu Formation, Sanju section. All sedimentary structures are consistent with a continental, predominantly alluvial facies, as interpreted by previous research on these formations.

Fig. 4. Petrography of sandstones and modern rivers draining from the northern margin of Tibet. (A) QFL plot (fields according to the sandstone classification and nomenclature of (Garzanti 2019)) Q= quartz, F= feldspar, L= lithic fragments. (B) Lithic fragments plot; Lm = metamorphic lithics, Lv= volcanic lithics, Ls= sedimentary lithics. Samples 15YK01, 15YK02 are modern sands collected from the upper Yulongkashi river, and SA17 was from the Sanju river in this study (see Fig. 1A for location). The samples with grey stars are published data. Sample 35 was collected from Kalakashi river (Rittner *et al*. 2016); samples 50, 54, 55 were collected from Yulongkashi river, Kalakashi river and Sanju river, respectively (Graham *et al*. 1993). Unlabelled symbols are new data from our sedimentary sections, from formations as denoted in the key. The sample locations are shown in Fig. 1.

Fig. 5. Normalized probability density plots (PDP) with histograms for detrital zircon U–Pb populations from our sedimentary sections (Kashitashi section, panel 7, and Sanju section, panels 5 and 6), compared to compiled data from potential source regions (panels 1–5).

Data from West Qiangtang (panel 1, P1) are from Ding *et al*. (2013), Gehrels *et al*. (2011), Pullen *et al*. (2008) and Zhu *et al*. (2011). Data from West Songpan-Ganzi – Tianshuihai (Panel 2, P2) are from Ding *et al*. (2013), Hu *et al*. (2016), Zhang *et al*. (2017) and Dong *et al*. (2019). Modern rivers draining the Karakoram and South Pamir, representing the potential hinterland provenance of the region west of the Karakoram fault (Panel 3, P3) use data from Zhuang *et al*. (2018). The Kalakashi and Yulongkashi Rivers draining Songpan-Ganzi – Tianshuihai and northern and southern WKL (Panel 4, P4) plot data from Rittner *et al*. (2016), Clift *et al*. (2017) and Blayney *et al*. (2019). Sanju River draining West Kunlun (Panel 5, P5) plots data from this study. Data from Sanju section (Panel 6, P6) are from Cao *et al*. (2015). The Kashitashi section, Panel 7 (P7) plots data from this study. Samples from this study are marked with a symbol *. Colours added to aid differentiation of panels (P1–7) as shown on right. Insets show 0–600 Ma sections of the plots in more detail.

Note that where source terrane compilations have relied heavily on detrital zircons of older sedimentary rocks (e.g. West Qiangtang, sedimentary rocks of Jurassic age and older; Songpan-Ganzi – Tianshuihai, sedimentary rocks of Late Triassic age and older), rather than igneous intrusions, younger populations may be under- or unrepresented. This is particularly true of the Songpan-Ganzi – Tianshuihai (P2) where zircons from Mesozoic intrusions are not represented in the compilation based on zircons in sedimentary rocks of Late Triassic age and older.

Fig. 6. A comparison of our new detrital zircon εHf(t) versus U–Pb ages with compiled published data from the West Kunlun, Pamir and Tianshuihai terranes (Zhang *et al*. 2023).

Fig. 7. Detrital rutile U–Pb ages presented as normalized probability density plots with histograms for the modern Sanju river, Sanju Section, and Kashitashi Section (sections A, B and C, as shown on Fig. 1C). Insets show the same data, 0–200 Ma, in expanded form.

Fig. 8. Fission-track versus U–Pb ages for double-dated single zircon grains from samples from Kashitashi and Sanju sections. Three grains (in samples KE210 and BK140) have ZFT ages older than their corresponding U–Pb ages at 1σ but lie on the 1:1 line at 2σ error, and are therefore not excluded from the plot. Samples with symbol * from the Sanju section are from Cao *et al*. (2015).

Fig. 9. Radial plots showing a subset of the zircon fission track data shown in Fig. 8 interpreted as representing exhumational signals. There is a considerable population of zircons with fission tracks too numerous to count in all samples. These cannot be represented on the radial plots. Samples from the Kashitashi section and the modern river at Sanju are from this study, and those from the Sanju section (symbol*) are from Cao *et al*. (2015). Using the same approach as Cao *et al*. (2015), the radial plots only include zircon grains for which ZFT ages are younger than the corresponding U–Pb ages, thereby excluding volcanic zircons. Samples KE95 and KE210 aliquot 1 (symbols #) do not have corresponding

U–Pb data and therefore all grains are plotted. The Eocene population in sample BK140 is required to be included in this exhumational plot because it meets the criteria in that a few grains in the population have ZFT ages younger than U–Pb age. However, the ZFT ages of these grains are only slightly younger than U–Pb age, and the majority of the grains in this population are volcanic (ZFT and U–Pb age within error). Therefore in all likelihood these grains are also volcanic.

Fig. 10. Radial plots showing the distribution of detrital apatite fission track ages, in samples from the Sanju section and Kashitashi section (sections A and C, see Fig 1C for location). Sample with symbol * is from the modern sand of the Yulongkashi river from Clift *et al*. (2017).

Fig. 11. Multidimensional Scaling (MDS) Plot (Vermeesch 2013) based on calculated K–S distances between zircon U–Pb age spectra, comparing Paleogene samples from Kashitashi section and Neogene samples from Sanju section, with potentially contributing hinterland source regions. West Kunlun (WKL, as characterised by modern Sanju River sand sample SA17), West Qiangtang, West Songpan-Ganzi – Tianshuihai and the region west of the Karakoram fault (Karakoram and South Pamir), and the Karakoram as detailed in Fig. 5. References as for Fig. 5, with bedrock Karakoram data from Zhuang *et al*. (2016) and references therein.

Fig. 12. A summary of new and published detrital zircon and apatite FT ages along strike from the Pamir to NW Tibet: From West to East: West Pamir (Panel A), data from Carrapa *et al*. (2014), Chapman *et al*. (2020) and Li *et al*. (2023); Northeast Pamir (Panel B), data from Carrapa *et al*. (2014); Aertashi section (Panel C, data from Blayney *et al*. (2019); Kekeya Section (Panel D), data from Cao *et al*. (2015); Keliyang Section (Panel E), data from Wang *et a*l. (2021); Sanju section (Panel F), zircon FT data from Cao *et al*. (2015), apatite FT data from this study; Kashitashi section (Panel G), data from this study. Section locations shown on Fig. 1. For ZFT data from this study, only populations detected as exhumational in origin on account of their ZFT ages being younger than U–Pb ages are included,

except for the Yulongkashi River samples (13062401, Clift *et al*. 2017) and KE95 where double-dating was not undertaken. Sample KE210 was not included in this figure because we interpret the ages as due to resetting by local fault reactivation. The Eocene ZFT population in sample BK140 (as shown by an asterisk) consists of 3 grains that narrowly fall off the 1:1 line (Fig. 8), in amongst a total population of 6 grains in this aged population, which fall on the 1:1 line, and are thus interpreted as of volcanic origin. Thus the 3 grains in the population in this figure, may also be recording a volcanic rather than exhumational signal. These data are also displayed as radial plots in Supplementary Info 10.

REFERENCES CITED

An, W., Hu, X.M., Garzanti, E., Wang, J.G., & Liu, Q., 2021. New Precise Dating of the India-Asia Collision in theTibetan Himalaya at 61 Ma, *Geophysical Research Letters*, **48**, e2020GL090641. https://doi.org/10.1029/2020GL090641

Blayney, T., Dupont-Nivet, G., Najman, Y., Proust, J.N., Meijer, N., Roperch, P., Sobel, E.R., Millar, I., & Guo, Z. 2019. Tectonic evolution of the Pamir recorded in the western Tarim Basin (China): sedimentologic and magnetostratigraphic analyses of the Aertashi section. *Tectonics*, **38**, 492–515. https://doi.org/10.1029/2018TC005146

Bosboom, R., Dupont-Nivet, G., Grothe, A., Brinkhuis, H., Villa, G., Mandic, O., Stoica, M., Kouwenhoven, T., Huang, W.T., Yang, W., & Guo, Z.J. 2014. Timing, cause and impact of the late Eocene stepwise sea retreat from the Tarim Basin (west China). *Palaeogeography Palaeoclimatology Palaeoecology*, **403**, 101–118. https://doi.org/10.1016/j.palaeo.2014.03.035

Bracciali, L., Parrish, R.R., Horstwood, M.S., Condon, D.J., & Najman, Y. 2013. UPb LA-(MC)-ICP-MS dating of rutile: New reference materials and applications to sedimentary provenance. *Chemical Geology*, **347**, 82–101. https://doi.org/10.1016/j.chemgeo.2013.03.013

Cao, K., Wang, G.C., Bernet, M., van der Beek, P., & Zhang, K.X. 2015. Exhumation history of the West Kunlun Mountains, northwestern Tibet: Evidence for a long-lived, rejuvenated orogen. *Earth and Planetary Science Letters*, **432**, 391–403. https://doi.org/10.1016/j.epsl.2015.10.033

Carrapa, B., Mustapha, F. S., Cosca, M., Gehrels, G., Schoenbohm, L. M., Sobel, E. R., DeCelles, P. G., Russell, J., & Goodman, P. 2014. Multisystem dating of modern river detritus from Tajikistan and China: Implications for crustal evolution and exhumation of the Pamir. *Lithosphere*, **6**, 443–455. https://doi.org/10.1130/L360.1

Chapman, J. B., Carrapa, B., DeCelles, P. G., Worthington, J., Mancin, N., Cobianchi, M., Stoica, M., Wang, X., Gadoev, M., & Oimahmadov, I. 2020. The Tajik Basin: A composite record of sedimentary basin evolution in response to tectonics in the Pamir. *Basin Research*, **32**, 525–545. https://doi.org/10.1111/bre.12381

Chapman, J. B., Robinson, A. C., Carrapa, B., Villarreal, D., Worthington, J., DeCelles, P. G., Kapp, P., Gadoev, M., Oimahmadov, I., & Gehrels, G. 2018. Cretaceous shortening and exhumation history of the South Pamir terrane. *Lithosphere*, **10**, 494–511. https://doi.org/10.1130/L691.1

Cheng, X., Chen, H., Lin, X., Wu, L., & Gong, J. 2017. Geometry and Kinematic Evolution of the Hotan-Tiklik Segment of the Western Kunlun Thrust Belt: Constrained by Structural Analyses and Apatite Fission Track Thermochronology. *The Journal of Geology*, **125**, 65–82. https://doi.org/10.1086/689187

Chung, S.L., Chu, M.F., Zhang, Y., Xie, Y., Lo, C.H., Lee, T.Y., Lan, C.Y., Li, X., Zhang, Q., & Wang, Y. 2005. Tibetan tectonic evolution inferred from spatial and temporal variations in post-collisional magmatism. *Earth Science Reviews*, **68**, 173–196. https://doi.org/10.1016/j.earscirev.2004.05.001

Clift, P. D., Mark, C., Alizai, A., Khan, H., & Jan, M. Q. 2022. Detrital U–Pb rutile and zircon data show Indus River sediment dominantly eroded from East Karakoram, not Nanga Parbat. *Earth and Planetary Science Letters*, **600**, 117873. https://doi.org/10.1016/j.epsl.2022.117873

Clift, P.D., Zheng, H., Carter, A., Böning, P., Jonell, T.N., Schorr, H., Shan, X., Pahnke, K., Wei, X., & Rittenour, T. 2017. Controls on erosion in the western Tarim Basin: Implications for the uplift of northwest Tibet and the Pamir. *Geosphere*, **13**, 1747–1765. https://doi.org/10.1130/GES01378.1

Compiling Group for Xinjiang Regional Stratigraphic Chart. 1981. Regional Stratigraphic Chart of Northwestern China, Branch of Xinjiang Uygur Autonomous Region. Geological Publishing House, Beijing (in Chinese), 346–402.

Cowgill, E. 2001. Tectonic evolution of the Altyn Tagh – Westerm Kunlun Fault System, Northwestern China. Unpublished PhD thesis, UCLA, USA.

Cui, J.T., Wang, J.C., Bian, X.W., Luo, Q.Z., Zhu, H.P., Wang, M.C., Chen, G.C. 2007. Zircon SHRIMP U-Pb dating of the Dongbake gneissic tonalite in northern Kangxiwar, West Kunlun. *Geological Bulletin of China*, **26**, 726–729.

Cui, J.T., Wang, J.C., Bian, X.W., Zhu, H.P., Yang K.J. 2006. Geological characteristics of Early Paleozoic amphibolite and tonalite in northern Kangxiwar, West Kunlun, China and their zircon SHRIMP U-Pb dating. *Geological Bulletin of China*, **25**, 1441–1449.

Deng, W.M. 1998. Cenozoic Intraplate Volcanic Rocks in the Northern Qinghai-Xizang Plateau. Geological Publishing House, Beijing, 19–26.

Dewey, J. F., Shackleton, R. M., Chengfa, C., & Yiyin, S. 1988. The tectonic evolution of the Tibetan Plateau. *Philosophical Transactions of the Royal Society of London. Series A, Mathematical and Physical Sciences*, **327**, 379–413. https://doi.org/10.1098/rsta.1988.0135

Ding, L., Kapp, P., Cai, F., Garzione, C. N., Xiong, Z., Wang, H., & Wang, C. 2022. Timing and mechanisms of Tibetan Plateau uplift. *Nature Reviews Earth & Environment*, **3**, 652–667. https://doi.org/10.1038/s43017-022-00318-4

Ding, L., Yang, D., Cai, F.L., Pullen, A., Kapp, P., Gehrels, G.E., Zhang, L.Y., Zhang, Q.H., Lai, Q.Z., & Yue, Y.H. 2013. Provenance analysis of the Mesozoic Hoh-Xil-Songpan-Ganzi turbidites in northern Tibet: Implications for the tectonic evolution of the eastern Paleo-Tethys Ocean. *Tectonics*, **32**, 34–48. https://doi.org/10.1002/tect.20013

Dong, R., Wang, H., Yan, Q. H., Zhang, X. Y., Wei, X. P., Li, P., & Zhou, K. L. 2019. Geochemical Characteristics and Zircon U-Pb Ages of the Bayankalashan Group in the Tianshihai Terrain of the West Kunlun Orogenic Belt: Implication for its Provenance and Tectonic Environment. *Geotecton. Metallog*, **43**, 1236–1257.

Force, E. R. 1980. The provenance of rutile. *Journal of Sedimentary Research*, **50**, 485–488. https://doi.org/10.1306/212F7A31-2B24-11D7-8648000102C1865D

Fraser, J.E., Searle, M.P., Parrish, R.R., and Noble, S.R. 2001. Chronology of deformation, metamorphism, and magmatism in the southern Karakoram Mountains. *Geological Society of America Bulletin*, **113**, 1443–1455. https://doi.org/10.1130/0016-7606(2001)113<1443:CODMAM>2.0.CO;2

Gain, S. E., Gréau, Y., Henry, H., Belousova, E., Dainis, I., Griffin, W. L., & O'reilly, S. Y. 2019. Mud Tank Zircon: Long-term evaluation of a reference material for U-Pb dating, Hf-isotope analysis and trace element analysis. *Geostandards and Geoanalytical Research*, **43**, 339–354. https://doi.org/10.1111/ggr.12265

Garzanti, E. 2019. Petrographic classification of sand and sandstone. *Earth-science reviews*, **192**, 545–563. https://doi.org/10.1016/j.earscirev.2018.12.014

Gehrels, G., Kapp, P., Decelles, P., Pullen, A., Blakey, R., Weislogel, A., Ding, L., Guynn, J., Martin, A., Mcquarrie, N., & Yin, A. 2011. Detrital zircon geochronology of pre-Tertiary strata in the Tibetan–Himalayan orogen. *Tectonics*, **TC5016**. https://doi.org/10.1029/2011TC002868

Graham, S., Hendrix, M., Wang, L., and Carroll, A. 1993. Collisional successor basins of western China: Impact of tectonic inheritance on sand composition. *Geological Society of America Bulletin*, **105**, 323–344, https://doi.org/10.1130/0016-7606(1993)105<0323:CSBOWC>2.3.CO;2

Hu, J., Wang, H., Huang, C., Tong, L., Mu, S., & Qiu, Z. 2016. Geological characteristics and age of the Dahongliutan Fe-ore deposit in the Western Kunlun orogenic belt, Xinjiang, northwestern China. *Journal of Asian Earth Sciences*, **116**, 1–25. https://doi.org/10.1016/j.jseaes.2015.08.014

Hu, X.M., Garzanti, E., Moore, T., & Raffi, I. 2015. Direct stratigraphic dating of India-Asia collision onset at the Selandian (middle Paleocene, 59 +/- 1 Ma). *Geology*, **43**, 859–862. https://doi.org/10.1130/G36872.1

Hu, X.M., Ma, A.L, Xue, W.W., Garzanti, E., Cao, Y., Li, S.M., Sun, G.Y., & Lai, W. 2022. Exploring a lost ocean in the Tibetan Plateau: Birth, growth, and demise of the Bangong-Nujiang Ocean. *Earth-Science Reviews*, **229**, 104031. https://doi.org/10.1016/j.earscirev.2022.104031

Hurford, A.J. 1990. Standardization of fission track dating calibration: Recommendation by the Fission Track Working Group of the IUGS Subcommission on Geochronology. *Chemical Geology, Isotope Geoscience Section*, **80**, 171–178. https://doi.org/10.1016/0168-9622(90)90025-8

Ingersoll, R.V., Bullard, T.F., Ford, R.L., Grimm, J.P., Pickle, J.D., & Sares, S.W. 1984. The effect of grain size on detrital modes: a test of the Gazzi-Dickinson point-counting method. *Journal of Sedimentary Research*, **54**, 103–116. https://doi.org/10.1306/212F83B9-2B24-11D7-8648000102C1865D

Jackson, S.E., Pearson, N.J., Griffin, W.L., & Belousova, E.A. 2004. The application of laser ablation-inductively coupled plasma-mass spectrometry to in situ U–Pb zircon geochronology. *Chemical Geology*, **211**, 47–69. https://doi.org/10.1016/j.chemgeo.2004.06.017

Kapp, P., & DeCelles, P. G. 2019. Mesozoic–Cenozoic geological evolution of the Himalayan-Tibetan orogen and working tectonic hypotheses. *American Journal of Science*, **319**, 159–254. https://doi.org/10.2475/03.2019.01

Lai, W., Hu, X.M., Garzanti, E., Sun, G.Y., Garzione, C.N., BouDagher-Fadel, M., & Ma, A.L. 2019. Initial growth of the Northern Lhasaplano, Tibetan Plateau in the early Late Cretaceous (ca. 92 Ma). *Geological Society of America Bulletin*, **131**, 1823–1836. https://doi.org/10.1130/B35124.1

Li, G., Sandiford, M., Fang, A., Kohn, B., Sandiford, D., Fu, B., Zhang, T., Cao, Y., & Chen, F. 2019. Multi-stage exhumation history of the West Kunlun orogen and the amalgamation of the Tibetan Plateau. *Earth and Planetary Science Letters*, **528**, 115833. https://doi.org/10.1016/j.epsl.2019.115833

Li, L., Najman, Y., Dupont-Nivet, G., Parra, M., Roperch, P., Kaya, M., Meijer, N., O'Sullivan, P., Jepson, G., & Aminov, J. 2023. Mesozoic–Cenozoic multistage tectonic evolution of the Pamir: Detrital fission-track constraints from the Tajik Basin. *Basin Research*, **35**, 530–550. https://doi.org/10.1111/bre.12721

Li, Y. P., Robinson, A. C., Gadoev, M., & Oimuhammadzoda, I. 2020. Was the Pamir salient built along a Late Paleozoic embayment on the southern Asian margin? *Earth and Planetary Science Letters*, **550**, 116554. https://doi.org/10.1016/j.epsl.2020.116554

Li, Y. P., Robinson, A. C., Zucali, M., Gadoev, M., Oimuhammadzoda, I., Lapen, T. J., & Carrapa, B. 2022. Mesozoic Tectonic Evolution in the Kurgovat‐Vanch Complex, NW Pamir. *Tectonics*, **41**, e2021TC007180. https://doi.org/10.1029/2021TC007180

Liu, D., Shi, R., Ding, L., Huang, Q., Zhang, X., Yue, Y., & Zhang, L. 2017. Zircon U–Pb age and Hf isotopic compositions of Mesozoic granitoids in southern Qiangtang, Tibet: implications for the subduction of the Bangong–Nujiang Tethyan Ocean. *Gondwana Research*, **41**, 157–172. https://doi.org/10.1016/j.gr.2015.04.007

Liu, Z., Jiang, Y.H., Jia, R.Y., Zhao, P., & Zhou, Q. 2015. Origin of Late Triassic high-K calc-alkaline granitoids and their potassic microgranular enclaves from the western Tibet Plateau, northwest China: Implications for Paleo-Tethys evolution. *Gondwana Research*, **27**, 326–341. https://doi.org/10.1016/j.gr.2013.09.022

Liu, Z., Jiang, Y.H., Jia, R.Y., Zhao, P., Zhou, Q., Wang, G.C., & Ni, C.Y. 2014. Origin of Middle Cambrian and Late Silurian potassic granitoids from the western Kunlun orogen, northwest China: a magmatic response to the Proto-Tethys evolution. *Mineralogy and Petrology*, **108**, 91–110. https://doi.org/10.1007/s00710-013-0288-0

Luvizotto, G., Zack, T., Meyer, H., Ludwig, T., Triebold, S., Kronz, A., Münker, C., Stockli, D., Prowatke, S., & Klemme, S. 2009. Rutile crystals as potential trace element and isotope mineral standards for microanalysis. *Chemical Geology*, **261**, 346–369. https://doi.org/10.1016/j.chemgeo.2008.04.012

Ma, A.L., Hu, X.M., Garzanti, E., Han, Z., & Lai, W. 2017. Sedimentary and tectonic evolution of the southern Qiangtang basin: implications for the Lhasa-Qiangtang collision timing. *Journal of Geophysical Research: Solid Earth*, **122**, 4790–4813. https://doi.org/10.1002/2017JB014211

Ma, A.L., Hu, X.M, Garzanti, E., Pullen, A., BouDagher-Fadel, M., Ji, X.K., Wang, J.G., Lai, W., & Xue., W.W. 2023. Mid-Cretaceous exhumation of the Central Qiangtang Mountain Range metamorphic rocks as evidenced by the Abushan continental redbeds, *Tectonics*, **42**, e2022TC007520. https://doi.org/10.1029/2022TC007520

Metcalfe, I. 1998. Palaeozoic and Mesozoic geological evolution of the SE Asian region: multidisciplinary constraints and implications for biogeography. *Biogeography and geological evolution of SE Asia*, 25–41.

Pan, G., Ding, J., Yao, D., & Wang, L. 2004. Geological map of the Qinghai-Xizang (Tibet) Plateau and adjacent areas, with guidebook. Chengdu, China, Cartographic Publishing House.

Pullen, A., Kapp, P., Gehrels, G.E., Vervoort, J.D., & Ding, L. 2008. Triassic continental subduction in central Tibet and Mediterranean-style closure of the Paleo-Tethys Ocean. *Geology*, **36**, 351–354. https://doi.org/10.1130/G24435A.1

Raterman, N. S., Robinson, A. C., & Cowgill, E. S. 2014. Structure and detrital zircon geochronology of the Domar fold-thrust belt: Evidence of pre-Cenozoic crustal thickening of the western Tibetan Plateau. *Geological Society of America Special Papers*, **507**, 89–104. https://doi.org/10.1130/2014.2507(05)

Rittner, M., Vermeesch, P., Carter, A., Bird, A., Stevens, T., Garzanti, E., Andò, S., Vezzoli, G., Dutt, R., & Xu, Z. 2016. The provenance of Taklamakan desert sand. *Earth and Planetary Science Letters*, **437**, 127–137. https://doi.org/10.1016/j.epsl.2015.12.036

Robinson, A. C. 2015. Mesozoic tectonics of the Gondwanan terranes of the Pamir plateau. *Journal of Asian Earth Sciences*, **102**, 170–179. https://doi.org/10.1016/j.jseaes.2014.09.012

Shanxi institute of geological survey. 2006. The 1:250,000 regional geological map in Qiaha area, P.R.C. Beijing, Geological Press.

Sharman, G.R. & Malkowski, M.A. 2020. Needles in a haystack: Detrital zircon U–Pb ages and the maximum depositional age of modern global sediment. *Earth-Science Reviews*, **203**, 103109. https://doi.org/10.1016/j.earscirev.2020.103109

Shi, G., Li, X., Li, Q., Chen, Z., Deng, J., Liu, Y., Kang, Z., Pang, E., Xu, Y., & Jia, X. 2012. Ion microprobe U-Pb age and Zr-in-rutile thermometry of rutiles from the Daixian rutile deposit in the Hengshan Mountains, Shanxi Province, China. *Economic Geology*, **107**, 525–535. https://doi.org/10.2113/econgeo.107.3.525

Sun, J.M., & Liu, T.S. 2006. The age of the Taklimakan Desert. *Science*, **312**, 1621. https://doi.org/10.1126/science.1124616

Sun, J.M., Windley, B.F., Zhang, Z.L., Fu, B.H., & Li, S.H. 2016. Diachronous seawater retreat from the southwestern margin of the Tarim Basin in the late Eocene. *Journal of Asian Earth Sciences*, **116**, 222–231. http://dx.doi.org/10.1016/j.jseaes.2015.11.020

Vermeesch, P. 2013. Multi-sample comparison of detrital age distributions. *Chemical Geology*, **341**, 140–146. https://doi.org/10.1016/j.chemgeo.2013.01.010

Vermeesch, P. 2009. Radialplotter: a java application for fission track, luminescence and other radial plots. *Radiation Measurements*, **44**, 409–410. https://doi.org/10.1016/j.radmeas.2009.05.003

Villarreal, D. P., Robinson, A. C., Chapman, J. B., Carrapa, B., Oimuhammadzoda, I., Gadoev, M., & Li, Y. 2023. Early Cretaceous displacement on the Tanymas thrust fault, Northern Pamir, Tajikistan, and regional tectonic implications. *Journal of Asian Earth Sciences: X*, **9**, 100147. https://doi.org/10.1016/j.jaesx.2023.100147

Wang, E., Wan, J., & Liu, J. 2003. Late Cenozoic geological evolution of the foreland basin bordering the West Kunlun range in Pulu area: Constraints on timing of uplift of northern margin of the Tibetan Plateau. *Journal of Geophysical Research: Solid Earth*, **108**, B8. https://doi.org/10.1029/2002JB001877

Wang, P., Liu, D., Li, H., Chevalier, M., Wang, Y., Pan, J., Zheng, Y., Ge, C., Bai, M., & Wang, S. 2021. Sedimentary provenance changes constrain the Eocene initial uplift of the Central Pamir, NW Tibetan Plateau. *Frontiers in Earth Science*, **9**, 741194. https://doi.org/10.3389/feart.2021.741194

Wei, X. P. 2018. Spatial-temporal Pattern, Petrogenesis and Tectonic Implications of the Triassic Granitoids from the Western Kunlun Orogen，Northwestern China. PhD. thesis, Guangzhou Institute of Geochemistry, Chinese Academy of Sciences, Guangzhou.

Wen, S., Sun, D., Yin, J., Chen, T., & Luo, H. 2000. Chapter 2: Stratigraphy. The Geological Formation and Evolution of the Karakorum and Kunlun Mountains. Chinese Science Publishing House, Beijing, 6–92.

Wiedenbeck, M. A., Alle, P. C., Corfu, P., Griffin, F., Meier, W. L., Oberli, M., Quadt, F. V., Roddick, J.C., & Spiegel, W. 1995. Three natural zircon standards for U-Th-Pb, Lu-Hf, trace element and

REE analyses. *Geostandards newsletter*, **19**, 1–23. https://doi.org/10.1111/j.1751-908X.1995.tb00147.x

Xiao, W. J., Windley, B. F., Liu, D. Y., Jian, P., Liu, C. Z., Yuan, C., & Sun, M. 2005. Accretionary tectonics of the Western Kunlun Orogen, China: a Paleozoic–Early Mesozoic, long-lived active continental margin with implications for the growth of Southern Eurasia. *The Journal of Geology*, **113**, 687–705. https://doi.org/10.1086/449326

Xue, W.W., Hu, X.M., Garzanti, E., Ma, A.L., Lai, W., & Li, C. 2023. Discriminating Qiangtang, Lhasa, and Himalayan sediment sources in the Tibetan Plateau by detrital-zircon U-Pb age and Hf isotope facies. *Earth-Science Reviews*, **236**, 104271. https://doi.org/10.1016/j.earscirev.2022.104271

Ye, H.M., Li, X.H., Li, Z.X., & Zhang, C.L. 2008. Age and origin of high Ba–Sr appinite–granites at the northwestern margin of the Tibet Plateau: Implications for early Paleozoic tectonic evolution of the Western Kunlun orogenic belt. *Gondwana Research*, **13**, 126–138. https://doi.org/10.1016/j.gr.2007.08.005

Zhang, C.L., Zou, H.B., Ye, X.T., & Chen, X.Y. 2018. Tectonic evolution of the West Kunlun Orogenic Belt along the northern margin of the Tibetan Plateau: Implications for the assembly of the Tarim terrane to Gondwana. *Geoscience Frontiers*, **10**, 973–988. https://doi.org/10.1016/j.gsf.2018.05.006

Zhang, L., Long, X., Zhang R., Dong, Y., Yuan, C., Xiao, W., & Wang Y. 2017. Source characteristics and provenance of metasedimentary rocks from the Kangxiwa Group in the Western Kunlun Orogenic Belt, NW China: Implications for tectonic setting and crustal growth. *Gondwana Research*, **46**, 43–56. http://dx.doi.org/10.1016/j.gr.2017.02.014

Zhang, S., Hu, X., Zhang, J., Li, Q., Xu, Y., Yu, Y., & Han, L. 2023. A database of detrital zircon U–Pb ages and Hf isotopic compositions from the Tarim, West Kunlun, Pamir, Tajik and Tianshuihai terranes. *Geoscience Data Journal*. Early View. https://doi.org/10.1002/gdj3.213

Zhang, Y., Niu, Y., Hu, Y., Liu, J., Ye, L., Kong, J., & Duan, M. 2016. The syncollisional granitoid magmatism and continental crust growth in the West Kunlun Orogen, China – Evidence from geochronology and geochemistry of the Arkarz pluton. *Lithos*, **245**, 191–204. https://doi.org/10.1016/j.lithos.2015.05.007

Zheng, H., Mcaulay Powell, C., An, Z., Zhou, J., & Dong, G. 2000. Pliocene uplift of the northern Tibetan Plateau. *Geology*, **28**, 715–718. https://doi.org/10.1130/0091-7613(2000)28<715:PUOTNT>2.0.CO;2

Zheng, H., Wei, X., Tada, R., Clift, P.D., Wang, B., Jourdan, F., Wang, P., & He, M. 2015. Late Oligocene-early Miocene birth of the Taklimakan Desert. *Proceedings of the National Academy of Sciences*, **112**, 7662–7667.

Zheng, H.B., Huang, X.T., & Butcher, K. 2006. Lithostratigraphy, petrography and facies analysis of the Late Cenozoic sediments in the foreland basin of the West Kunlun. *Palaeogeography Palaeoclimatology Palaeoecology*, **241**, 61–78. https://doi.org/10.1016/j.palaeo.2006.06.015

Zhu, D.C., Zhao, Z.D., Niu, Y., Dilek, Y., & Mo, X.X. 2011. Lhasa terrane in southern Tibet came from Australia. *Geology*, **39**, 727–730. https://doi.org/10.1130/G31895.1

Zhuang, G., Najman, Y., Tian, Y., Carter, A., Gemignani, L., Wijbrans, J., Jan, M.Q., & Khan, M.A. 2018. Insights into the evolution of the Hindu Kush–Kohistan–Karakoram from modern river sand detrital geo-and thermochronological studies. *Journal of the Geological Society*, **175**, 934–948. https://doi.org/10.1144/jgs2018-007

Fig. 1

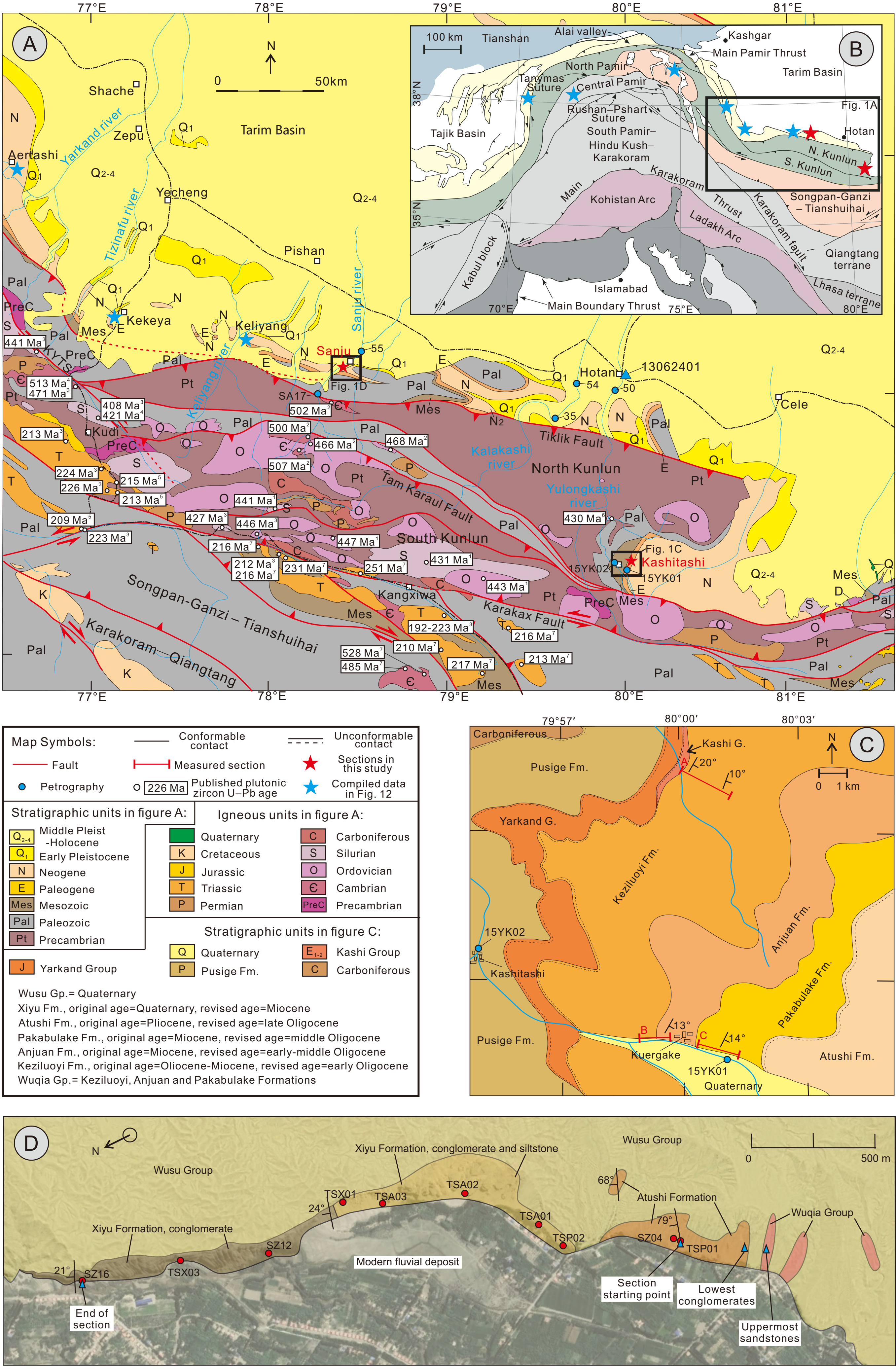
A
B
C
D
Tarim Basin
Shache
Zepu
Aertashi
Yarkand river
Yecheng
Tizinafu river
Pishan
Kekeya
Keliyang
Keliyang river
Sanju
Sanju river
Fig. 1D
SA17
Hotan
13062401
Cele
Kudi
Tiklik Fault
North Kunlun
Kalakashi river
Yulongkashi river
Tam Karaul Fault
South Kunlun
Kangxiwa
Karakax Fault
Fig. 1C
Kashitashi
15YK02
15YK01
Songpan-Ganzi – Tianshuihai
Karakoram–Qiangtang
KYTS
0 50km
N
77°E
78°E
79°E
80°E
81°E
37°N
36°N
Tianshan
Alai valley
Kashgar
Main Pamir Thrust
North Pamir
Tanymas Suture
Central Pamir
Rushan–Pshart Suture
South Pamir–Hindu Kush–Karakoram
Tajik Basin
Fig. 1A
N. Kunlun
S. Kunlun
Songpan-Ganzi – Tianshuihai
Karakoram Thrust
Main Karakoram Thrust
Kohistan Arc
Ladakh Arc
Karakoram fault
Qiangtang terrane
Lhasa terrane
Kabul block
Islamabad
Main Boundary Thrust
100 km
38°N
35°N
70°E
75°E
80°E
Map Symbols:
Conformable contact
Unconformable contact
Fault
Measured section
Sections in this study
Petrography
Published plutonic zircon U–Pb age
Compiled data in Fig. 12
Stratigraphic units in figure A:
Middle Pleist -Holocene
Early Pleistocene
Neogene
Paleogene
Mesozoic
Paleozoic
Precambrian
Yarkand Group
Igneous units in figure A:
Quaternary
Cretaceous
Jurassic
Triassic
Permian
Carboniferous
Silurian
Ordovician
Cambrian
Precambrian
Stratigraphic units in figure C:
Quaternary
Pusige Fm.
Kashi Group
Carboniferous
Wusu Gp.= Quaternary
Xiyu Fm., original age=Quaternary, revised age=Miocene
Atushi Fm., original age=Pliocene, revised age=late Oligocene
Pakabulake Fm., original age=Miocene, revised age=middle Oligocene
Anjuan Fm., original age=Miocene, revised age=early-middle Oligocene
Keziluoyi Fm., original age=Oliocene-Miocene, revised age=early Oligocene
Wuqia Gp.= Keziluoyi, Anjuan and Pakabulake Formations
79°57′
80°00′
80°03′
36°22′
36°18′
Carboniferous
Pusige Fm.
Kashi G.
Yarkand G.
Keziluoyi Fm.
Anjuan Fm.
Pakabulake Fm.
Atushi Fm.
Kuergake
Quaternary
0 1 km
Wusu Group
Xiyu Formation, conglomerate and siltstone
Xiyu Formation, conglomerate
Atushi Formation
Wuqia Group
Modern fluvial deposit
Section starting point
Lowest conglomerates
Uppermost sandstones
End of section
TSX01
TSA03
TSA02
TSA01
TSP02
SZ04
TSP01
SZ12
SZ16
TSX03
0 500 m

Fig. 2

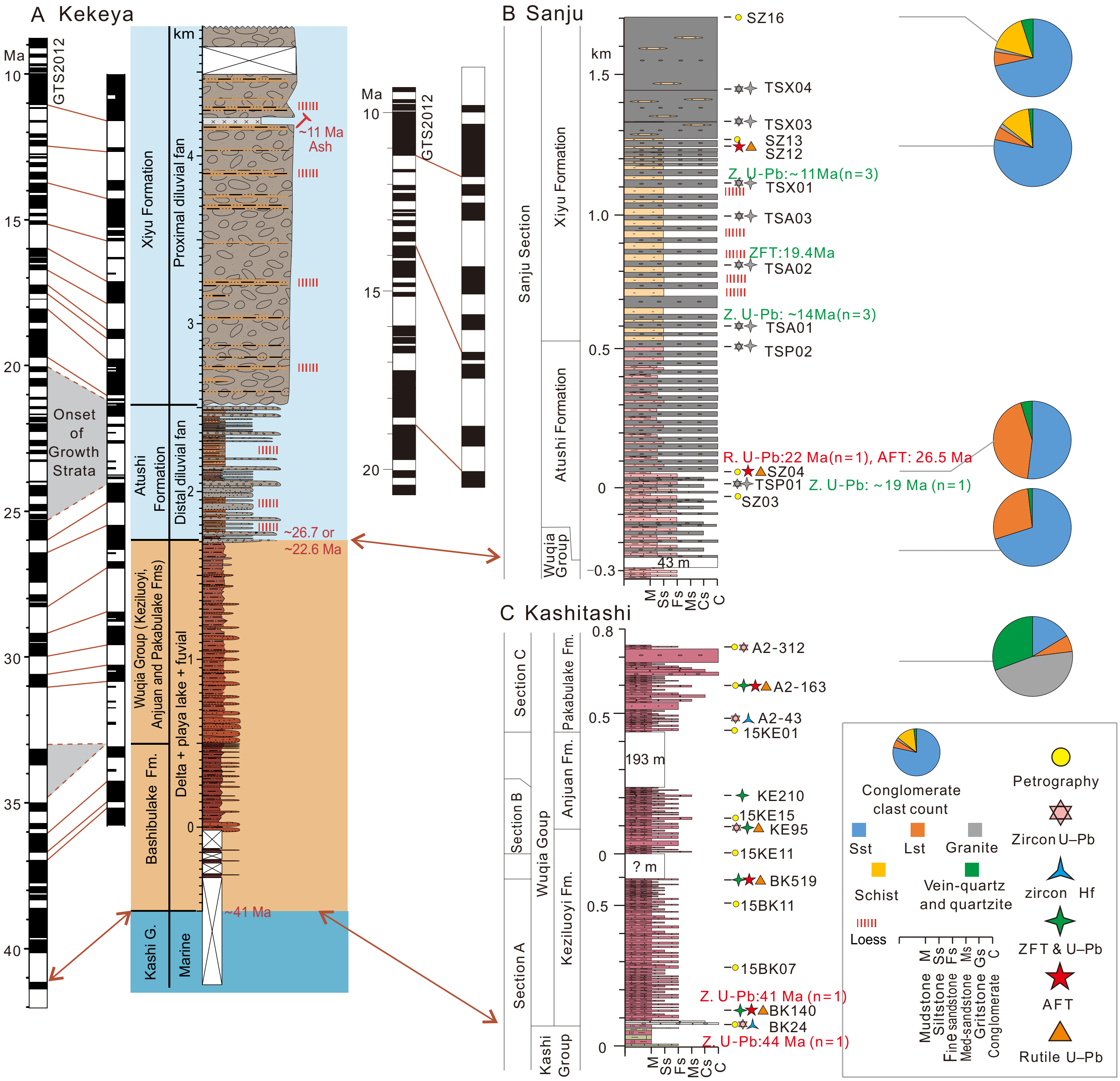
A Kekeya
Ma
GTS2012
km
Xiyu Formation
Proximal diluvial fan
~11 Ma
Ash
Onset
of
Growth
Strata
Atushi
Formation
Distal diluvial fan
~26.7 or
~22.6 Ma
Wuqia Group (Keziluoyi, Anjuan and Pakabulake Fms)
Bashibulake Fm.
Delta + playa lake + fuvial
~41 Ma
Kashi G.
Marine
B Sanju
Sanju Section
Xiyu Formation
Atushi Formation
Wuqia Group
43 m
SZ16
TSX04
TSX03
SZ13
SZ12
Z. U-Pb:~11Ma(n=3)
TSX01
TSA03
ZFT:19.4Ma
TSA02
Z. U-Pb: ~14Ma(n=3)
TSA01
TSP02
R. U-Pb:22 Ma(n=1), AFT: 26.5 Ma
SZ04
TSP01
Z. U-Pb: ~19 Ma (n=1)
SZ03
C Kashitashi
Section C
Section B
Section A
Wuqia Group
Kashi Group
Pakabulake Fm.
Anjuan Fm.
Keziluoyi Fm.
193 m
? m
A2-312
A2-163
A2-43
15KE01
KE210
15KE15
KE95
15KE11
BK519
15BK11
15BK07
Z. U-Pb:41 Ma (n=1)
BK140
BK24
Z. U-Pb:44 Ma (n=1)
M Ss Fs Ms Cs C
Conglomerate clast count
Sst
Lst
Granite
Schist
Vein-quartz and quartzite
Loess
Mudstone
Siltstone
Fine sandstone
Med-sandstone
Gritstone
Conglomerate
Petrography
Zircon U–Pb
zircon Hf
ZFT & U–Pb
AFT
Rutile U–Pb

Fig. 3

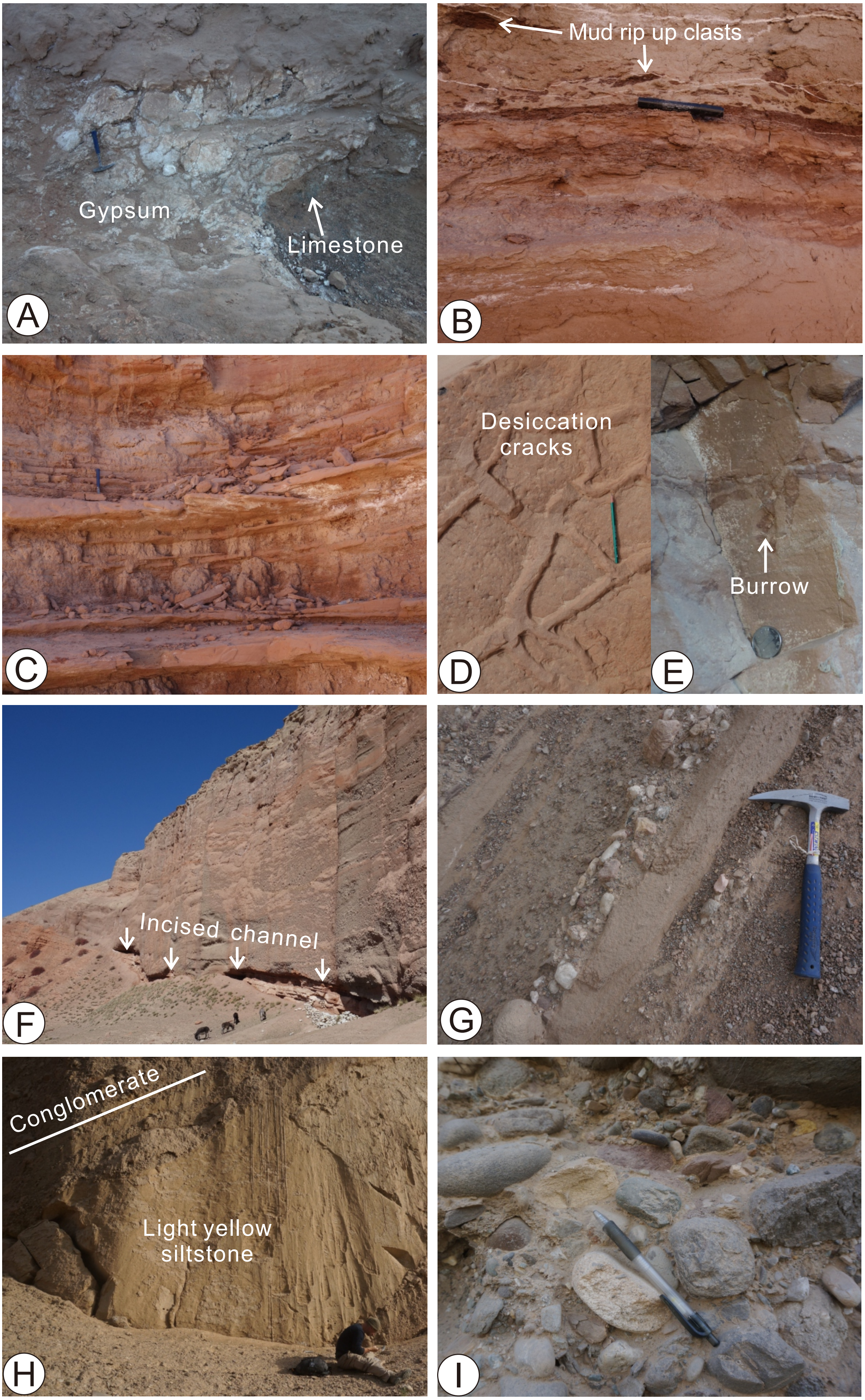
Gypsum
Limestone
A
Mud rip up clasts
B
C
Desiccation cracks
D
Burrow
E
Incised channel
F
G
Conglomerate
Light yellow siltstone
H
I

Fig. 4

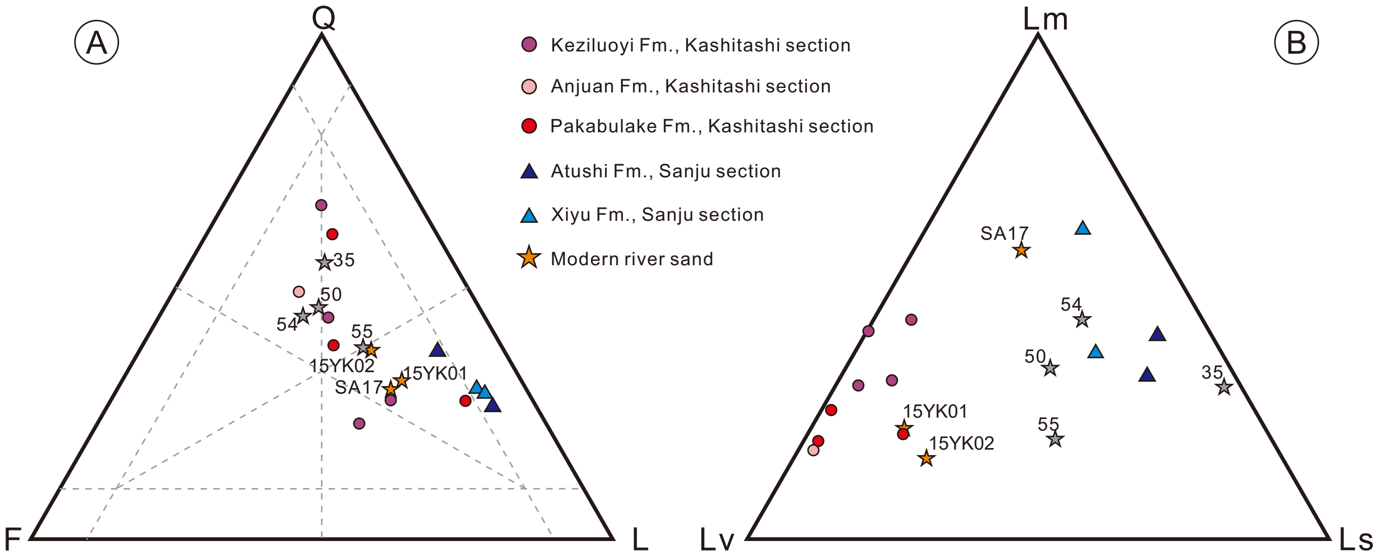
A
Q
F
L
35
50
54
55
15YK02
15YK01
SA17
Keziluoyi Fm., Kashitashi section
Anjuan Fm., Kashitashi section
Pakabulake Fm., Kashitashi section
Atushi Fm., Sanju section
Xiyu Fm., Sanju section
Modern river sand
B
Lm
Lv
Ls
SA17
54
50
35
55
15YK01
15YK02

Fig. 5

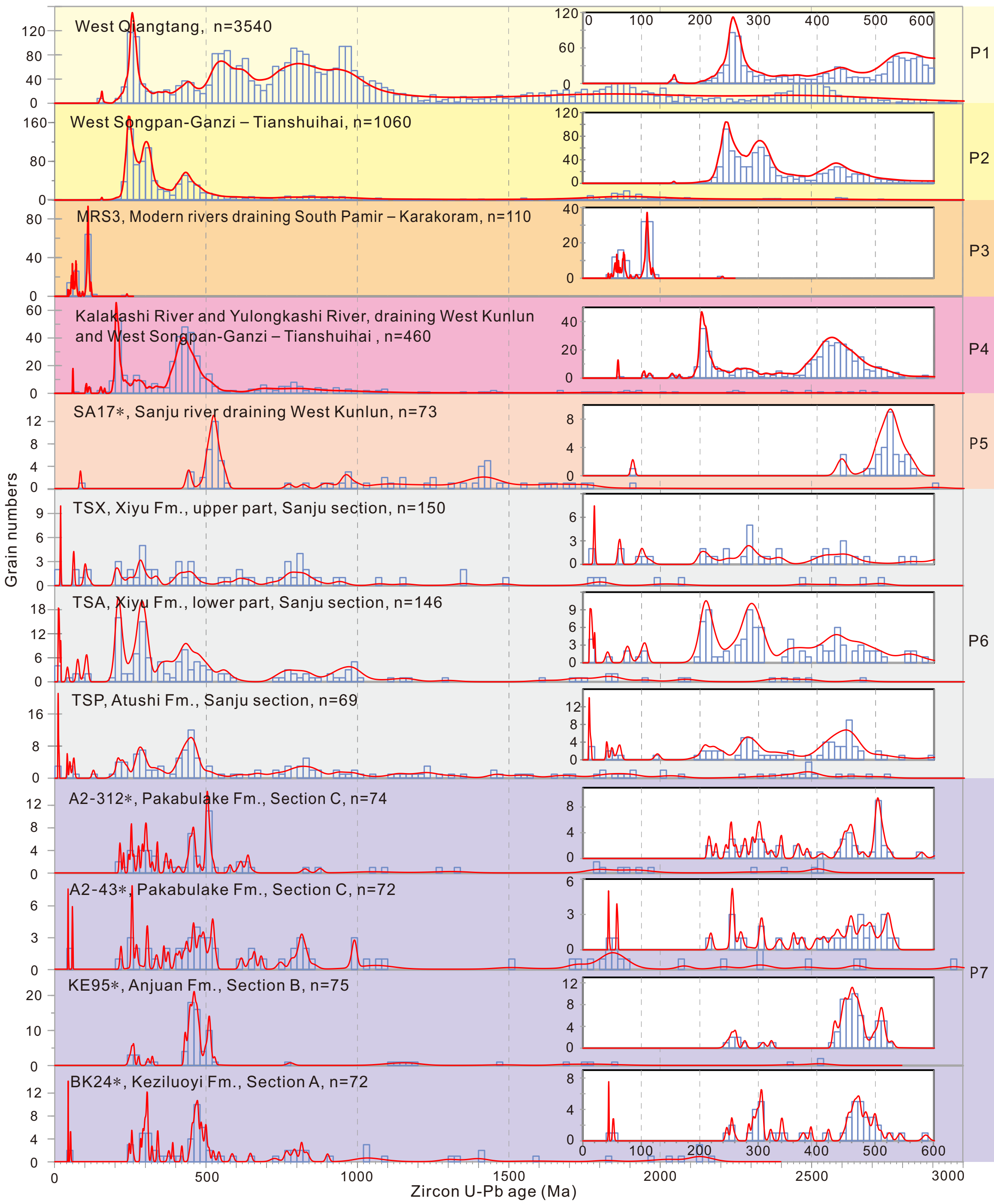
West Qiangtang, n=3540
West Songpan-Ganzi – Tianshuihai, n=1060
MRS3, Modern rivers draining South Pamir – Karakoram, n=110
Kalakashi River and Yulongkashi River, draining West Kunlun and West Songpan-Ganzi – Tianshuihai , n=460
SA17*, Sanju river draining West Kunlun, n=73
TSX, Xiyu Fm., upper part, Sanju section, n=150
TSA, Xiyu Fm., lower part, Sanju section, n=146
TSP, Atushi Fm., Sanju section, n=69
A2-312*, Pakabulake Fm., Section C, n=74
A2-43*, Pakabulake Fm., Section C, n=72
KE95*, Anjuan Fm., Section B, n=75
BK24*, Keziluoyi Fm., Section A, n=72
P1
P2
P3
P4
P5
P6
P7
Grain numbers
Zircon U-Pb age (Ma)
0
500
1000
1500
2000
2500
3000
100
200
300
400
600

Fig. 6

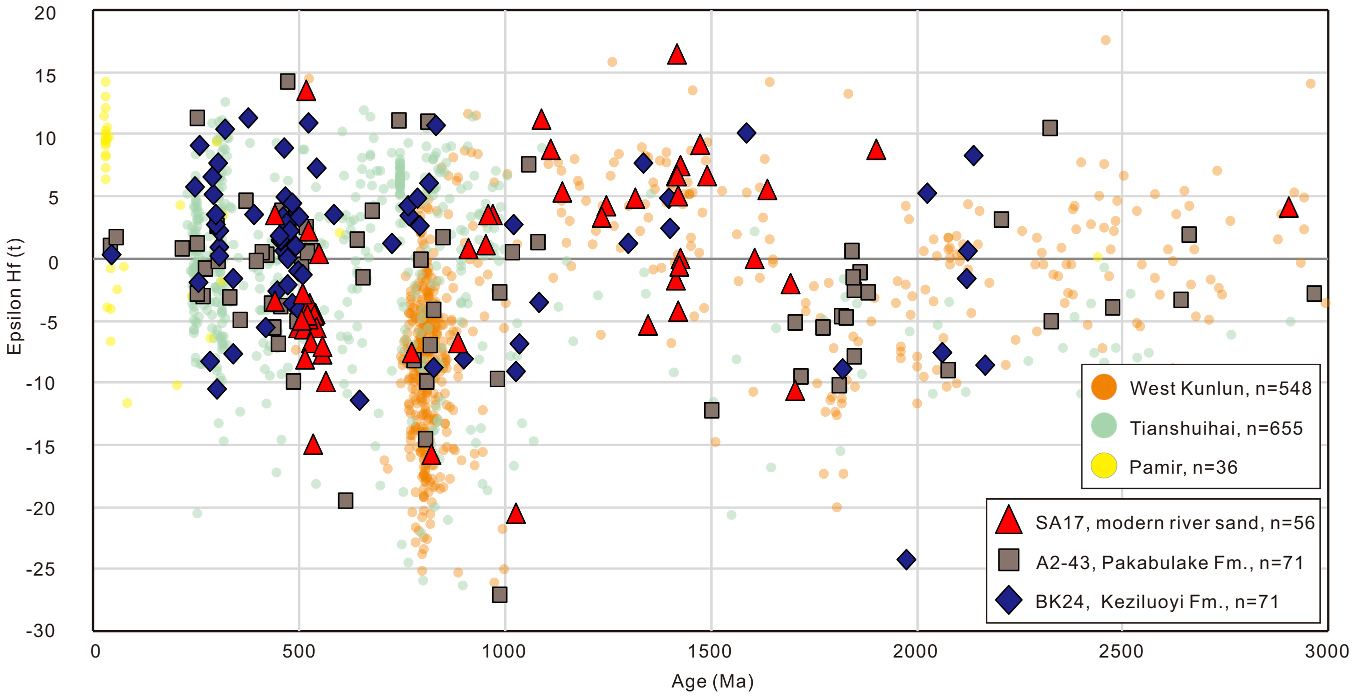

20
15
10
5
0
-5
-10
-15
-20
-25
-30
Epsilon Hf (t)
0
500
1000
1500
2000
2500
3000
Age (Ma)
West Kunlun, n=548
Tianshuihai, n=655
Pamir, n=36
SA17, modern river sand, n=56
A2-43, Pakabulake Fm., n=71
BK24, Keziluoyi Fm., n=71

Fig. 7

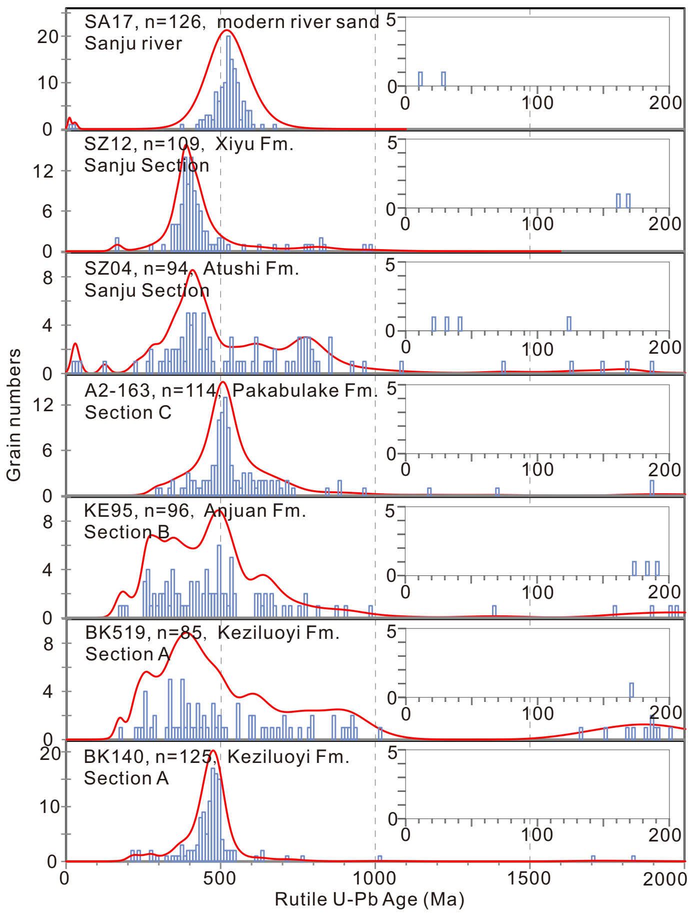

SA17, n=126, modern river sand
Sanju river
SZ12, n=109, Xiyu Fm.
Sanju Section
SZ04, n=94, Atushi Fm.
Sanju Section
A2-163, n=114, Pakabulake Fm.
Section C
KE95, n=96, Anjuan Fm.
Section B
BK519, n=85, Keziluoyi Fm.
Section A
BK140, n=125, Keziluoyi Fm.
Section A
Grain numbers
Rutile U-Pb Age (Ma)
0
500
1000
1500
2000
100
200

Fig. 8

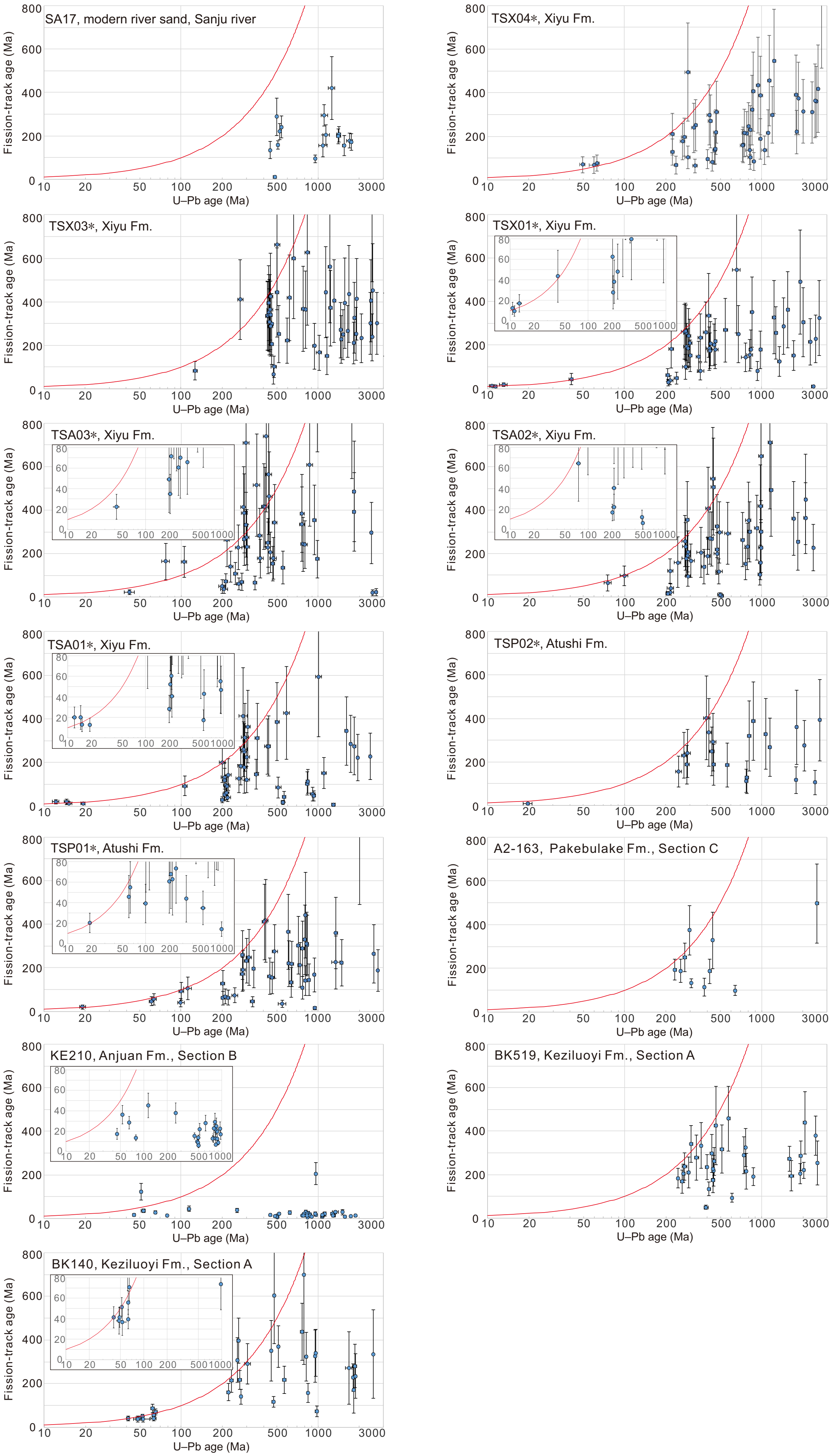
SA17, modern river sand, Sanju river
TSX04∗, Xiyu Fm.
TSX03∗, Xiyu Fm.
TSX01∗, Xiyu Fm.
TSA03∗, Xiyu Fm.
TSA02∗, Xiyu Fm.
TSA01∗, Xiyu Fm.
TSP02∗, Atushi Fm.
TSP01∗, Atushi Fm.
A2-163, Pakebulake Fm., Section C
KE210, Anjuan Fm., Section B
BK519, Keziluoyi Fm., Section A
BK140, Keziluoyi Fm., Section A
Fission-track age (Ma)
U–Pb age (Ma)

Fig. 9

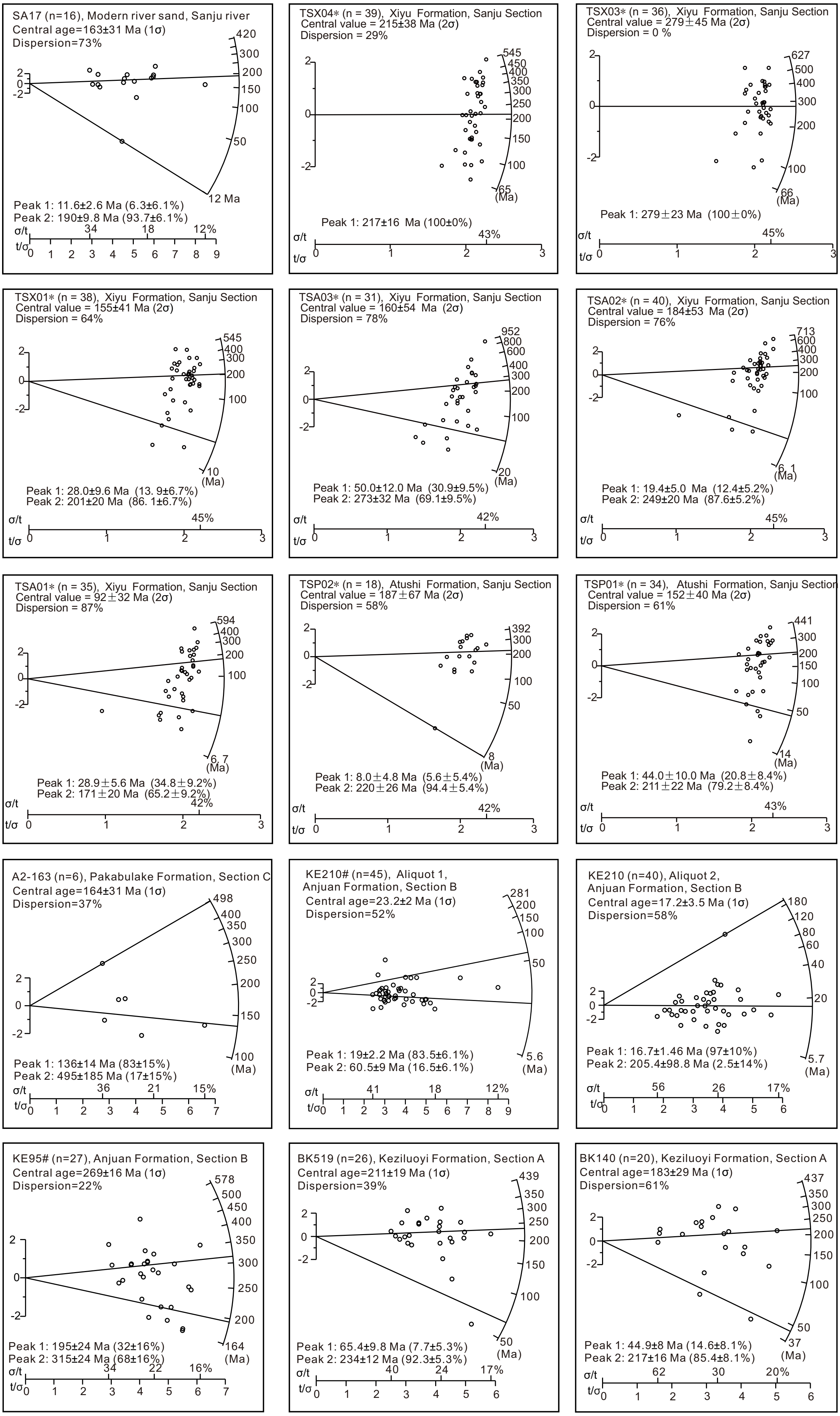
SA17 (n=16), Modern river sand, Sanju river
Central age=163±31 Ma (1σ)
Dispersion=73%
Peak 1: 11.6±2.6 Ma (6.3±6.1%)
Peak 2: 190±9.8 Ma (93.7±6.1%)
TSX04* (n = 39), Xiyu Formation, Sanju Section
Central value = 215±38 Ma (2σ)
Dispersion = 29%
Peak 1: 217±16 Ma (100±0%)
TSX03* (n = 36), Xiyu Formation, Sanju Section
Central value = 279±45 Ma (2σ)
Dispersion = 0 %
Peak 1: 279±23 Ma (100±0%)
TSX01* (n = 38), Xiyu Formation, Sanju Section
Central value = 155±41 Ma (2σ)
Dispersion = 64%
Peak 1: 28.0±9.6 Ma (13.9±6.7%)
Peak 2: 201±20 Ma (86.1±6.7%)
TSA03* (n = 31), Xiyu Formation, Sanju Section
Central value = 160±54 Ma (2σ)
Dispersion = 78%
Peak 1: 50.0±12.0 Ma (30.9±9.5%)
Peak 2: 273±32 Ma (69.1±9.5%)
TSA02* (n = 40), Xiyu Formation, Sanju Section
Central value = 184±53 Ma (2σ)
Dispersion = 76%
Peak 1: 19.4±5.0 Ma (12.4±5.2%)
Peak 2: 249±20 Ma (87.6±5.2%)
TSA01* (n = 35), Xiyu Formation, Sanju Section
Central value = 92±32 Ma (2σ)
Dispersion = 87%
Peak 1: 28.9±5.6 Ma (34.8±9.2%)
Peak 2: 171±20 Ma (65.2±9.2%)
TSP02* (n = 18), Atushi Formation, Sanju Section
Central value = 187±67 Ma (2σ)
Dispersion = 58%
Peak 1: 8.0±4.8 Ma (5.6±5.4%)
Peak 2: 220±26 Ma (94.4±5.4%)
TSP01* (n = 34), Atushi Formation, Sanju Section
Central value = 152±40 Ma (2σ)
Dispersion = 61%
Peak 1: 44.0±10.0 Ma (20.8±8.4%)
Peak 2: 211±22 Ma (79.2±8.4%)
A2-163 (n=6), Pakabulake Formation, Section C
Central age=164±31 Ma (1σ)
Dispersion=37%
Peak 1: 136±14 Ma (83±15%)
Peak 2: 495±185 Ma (17±15%)
KE210# (n=45), Aliquot 1,
Anjuan Formation, Section B
Central age=23.2±2 Ma (1σ)
Dispersion=52%
Peak 1: 19±2.2 Ma (83.5±6.1%)
Peak 2: 60.5±9 Ma (16.5±6.1%)
KE210 (n=40), Aliquot 2,
Anjuan Formation, Section B
Central age=17.2±3.5 Ma (1σ)
Dispersion=58%
Peak 1: 16.7±1.46 Ma (97±10%)
Peak 2: 205.4±98.8 Ma (2.5±14%)
KE95# (n=27), Anjuan Formation, Section B
Central age=269±16 Ma (1σ)
Dispersion=22%
Peak 1: 195±24 Ma (32±16%)
Peak 2: 315±24 Ma (68±16%)
BK519 (n=26), Keziluoyi Formation, Section A
Central age=211±19 Ma (1σ)
Dispersion=39%
Peak 1: 65.4±9.8 Ma (7.7±5.3%)
Peak 2: 234±12 Ma (92.3±5.3%)
BK140 (n=20), Keziluoyi Formation, Section A
Central age=183±29 Ma (1σ)
Dispersion=61%
Peak 1: 44.9±8 Ma (14.6±8.1%)
Peak 2: 217±16 Ma (85.4±8.1%)
σ/t
t/σ
(Ma)

Fig. 10

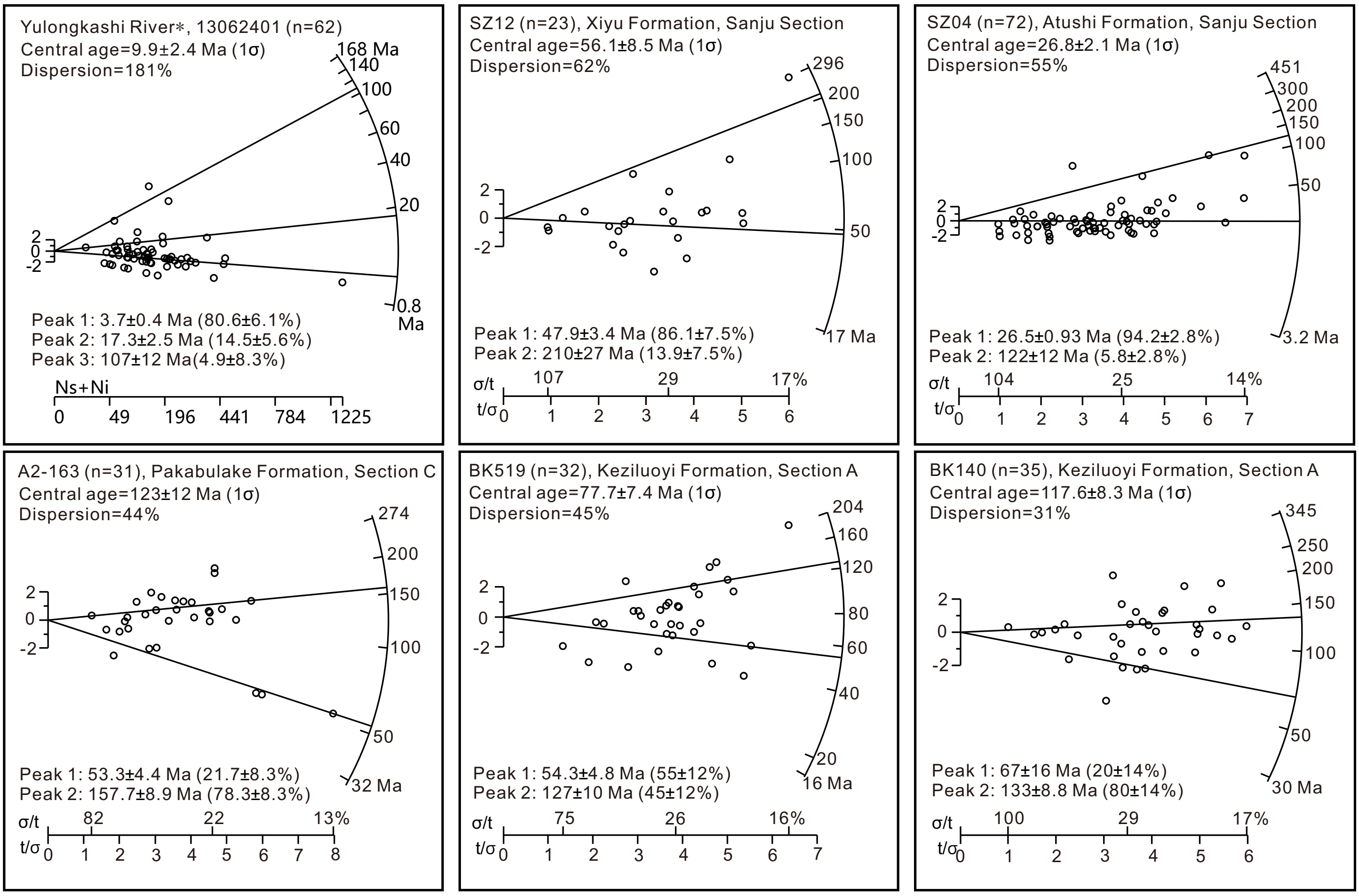
Yulongkashi River*, 13062401 (n=62)
Central age=9.9±2.4 Ma (1σ)
Dispersion=181%
168 Ma
140
100
60
40
20
0.8 Ma
2
0
-2
Peak 1: 3.7±0.4 Ma (80.6±6.1%)
Peak 2: 17.3±2.5 Ma (14.5±5.6%)
Peak 3: 107±12 Ma(4.9±8.3%)
Ns+Ni
0
49
196
441
784
1225
SZ12 (n=23), Xiyu Formation, Sanju Section
Central age=56.1±8.5 Ma (1σ)
Dispersion=62%
296
200
150
100
50
17 Ma
2
0
-2
Peak 1: 47.9±3.4 Ma (86.1±7.5%)
Peak 2: 210±27 Ma (13.9±7.5%)
σ/t
107
29
17%
t/σ
0 1 2 3 4 5 6
SZ04 (n=72), Atushi Formation, Sanju Section
Central age=26.8±2.1 Ma (1σ)
Dispersion=55%
451
300
200
150
100
50
3.2 Ma
2
0
-2
Peak 1: 26.5±0.93 Ma (94.2±2.8%)
Peak 2: 122±12 Ma (5.8±2.8%)
σ/t
104
25
14%
t/σ
0 1 2 3 4 5 6 7
A2-163 (n=31), Pakabulake Formation, Section C
Central age=123±12 Ma (1σ)
Dispersion=44%
274
200
150
100
50
32 Ma
2
0
-2
Peak 1: 53.3±4.4 Ma (21.7±8.3%)
Peak 2: 157.7±8.9 Ma (78.3±8.3%)
σ/t
82
22
13%
t/σ
0 1 2 3 4 5 6 7 8
BK519 (n=32), Keziluoyi Formation, Section A
Central age=77.7±7.4 Ma (1σ)
Dispersion=45%
204
160
120
80
60
40
20
16 Ma
2
0
-2
Peak 1: 54.3±4.8 Ma (55±12%)
Peak 2: 127±10 Ma (45±12%)
σ/t
75
26
16%
t/σ
0 1 2 3 4 5 6 7
BK140 (n=35), Keziluoyi Formation, Section A
Central age=117.6±8.3 Ma (1σ)
Dispersion=31%
345
250
200
150
100
50
30 Ma
2
0
-2
Peak 1: 67±16 Ma (20±14%)
Peak 2: 133±8.8 Ma (80±14%)
σ/t
100
29
17%
t/σ
0 1 2 3 4 5 6

Fig. 11

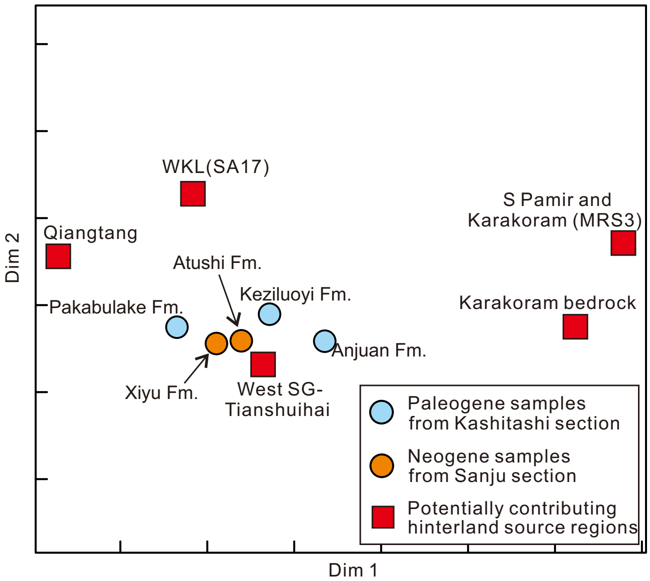
WKL(SA17)
S Pamir and
Karakoram (MRS3)
Qiangtang
Atushi Fm.
Keziluoyi Fm.
Karakoram bedrock
Pakabulake Fm.
Anjuan Fm.
Xiyu Fm.
West SG-
Tianshuihai
Paleogene samples
from Kashitashi section
Neogene samples
from Sanju section
Potentially contributing
hinterland source regions
Dim 2
Dim 1

Fig. 12

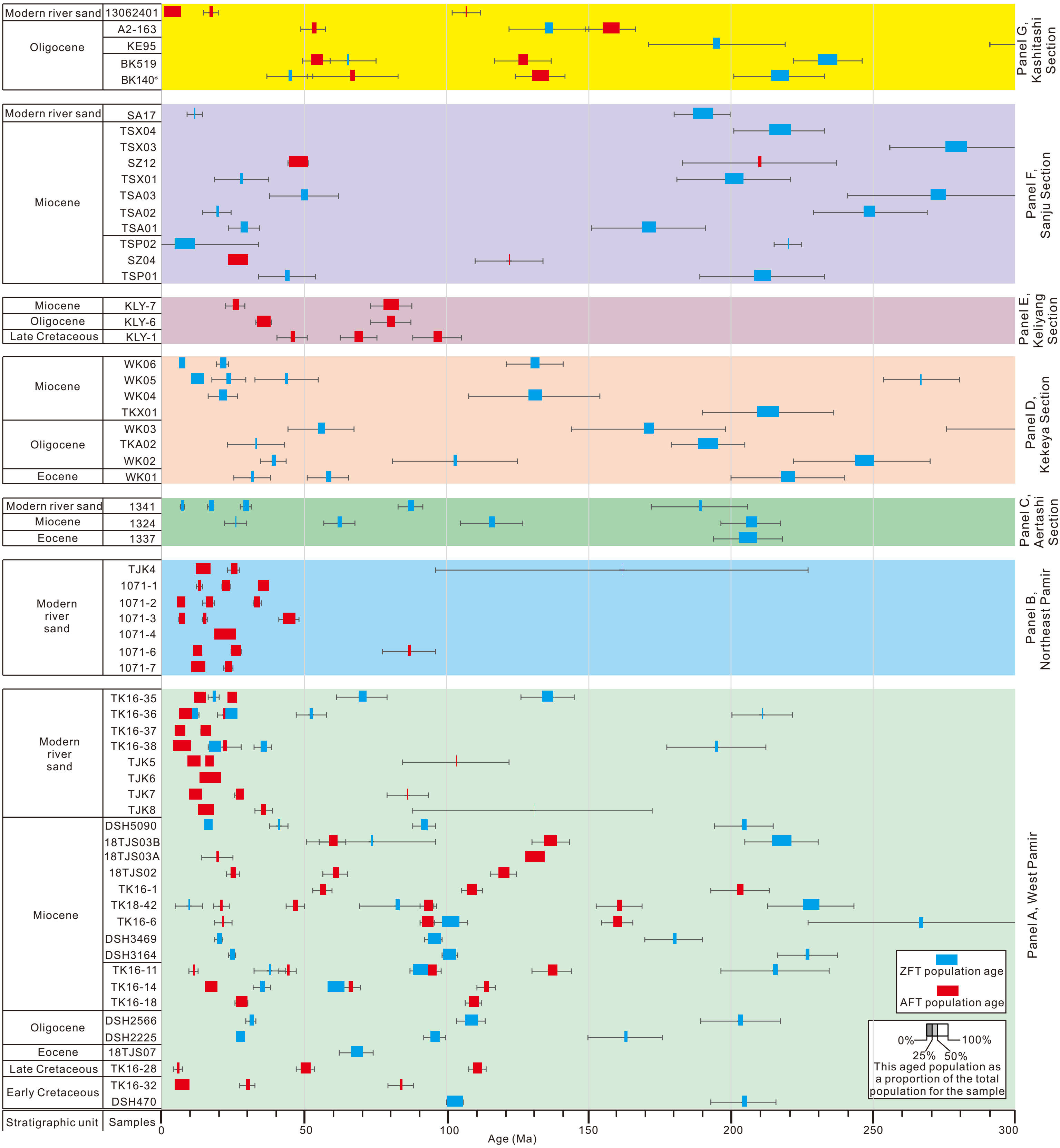
Stratigraphic unit
Samples
Modern river sand
13062401
Oligocene
A2-163
KE95
BK519
BK140*
Panel G, Kashitashi Section
SA17
Miocene
TSX04
TSX03
SZ12
TSX01
TSA03
TSA02
TSA01
TSP02
SZ04
TSP01
Panel F, Sanju Section
KLY-7
KLY-6
Late Cretaceous
KLY-1
Panel E, Keliyang Section
WK06
WK05
WK04
TKX01
WK03
TKA02
WK02
Eocene
WK01
Panel D, Kekeya Section
1341
1324
1337
Panel C, Aertashi Section
TJK4
1071-1
1071-2
1071-3
1071-4
1071-6
1071-7
Panel B, Northeast Pamir
TK16-35
TK16-36
TK16-37
TK16-38
TJK5
TJK6
TJK7
TJK8
DSH5090
18TJS03B
18TJS03A
18TJS02
TK16-1
TK18-42
TK16-6
DSH3469
DSH3164
TK16-11
TK16-14
TK16-18
DSH2566
DSH2225
18TJS07
TK16-28
Early Cretaceous
TK16-32
DSH470
Panel A, West Pamir
ZFT population age
AFT population age
0%
25%
50%
100%
This aged population as a proportion of the total population for the sample
0
50
100
150
200
250
300
Age (Ma)